

Mechanical Properties and Corrosion Behavior of Wire Arc Additive Manufactured ER5356 Al Alloys

M.Tech. Thesis

By
Abhinav Singhal



**DEPARTMENT OF METALLURGICAL
ENGINEERING AND MATERIALS SCIENCE
INDIAN INSTITUTE OF TECHNOLOGY
INDORE
MAY, 2024**

Mechanical Properties and Corrosion Behavior of Wire Arc Additive Manufactured ER5356 Al Alloys

A THESIS

*Submitted in partial fulfillment of the
requirements for the award of the degree
of*
Master of Technology

Submitted by
Abhinav Singhal
(2202105024)

Under the guidance of
Dr. Hemant Borkar
Dr. Ajay Kumar Kushwaha



**DEPARTMENT OF METALLURGICAL
ENGINEERING AND MATERIALS SCIENCE
INDIAN INSTITUTE OF TECHNOLOGY
INDORE**

MAY, 2024



INDIAN INSTITUTE OF TECHNOLOGY INDORE

CANDIDATE'S DECLARATION

I hereby certify that the work which is being presented in the thesis entitled **Mechanical properties and corrosion behavior of wire arc additive manufactured ER5356 Al alloys** in the partial fulfilment of the requirements for the award of the degree of **MASTER OF TECHNOLOGY** and submitted in the **DEPARTMENT OF METALLURGICAL ENGINEERING AND MATERIALS SCIENCE, Indian Institute of Technology Indore**, is an authentic record of my own work carried out during the time period from July 2023 to June 2024 under the supervision of Dr. Hemant Borkar and Dr. Ajay Kumar Kushwaha, Department of MEMS, Indian Institute of Technology, Indore.

The matter presented in this thesis has not been submitted by me for the award of any other degree of this or any other institute.

Abhinav Singhal

23/05/2024

This is to certify that the above statement made by the candidate is correct to the best of my/our knowledge.

Dr. Hemant Borkar

Dr. Ajay Kumar Kushwaha

Abhinav Singhal has successfully given his M.Tech. Oral Examination held on **28/05/2024**.

Dr. Hemant Borkar
Asst. Professor, IIT Indore
Date: 30/05/2024

Convener, DPGC
Dept. of MEMS
Date: 30/05/2024

Acknowledgement

Firstly, I would like to thank my supervisor, Dr. Hemant Borkar, for considering me worthy enough to work under him on this project. I thank him for giving me the opportunity and all the necessary support to study wire arc additive manufacturing of Aluminium alloys.

My sincerest gratitude to my co-supervisor, Dr. Ajay Kumar Kushwaha, for taking time to assess my work and utilizing their immense knowledge to provide constructive criticism for obtaining the desired results to achieve the said objectives. I am also extremely grateful to the DPGC, Dr. Dharendra Kumar Rai, for allowing me to utilize the various academic resources and department facilities at our disposal.

Then, I would like to thank Mr. Ankush Marodkar, Mr. Hitesh Patil and Mr. Akshay Kumar for handing me the first torch in the darkness of the field of Research in WAAM and Corrosion. This couldn't have been completed without their guidance.

I would also like to thank my friends, Musaab, Aman, Sudharshana, and Ramamoorthy, who supported me in the toughest of times.

And lastly, I would like to thank those hundreds of scholars who have previously researched and contributed to this field, on whose works this report is based.

With sincerest regards,



Abhinav Singhal

Dedicated to my parents, whose unwavering support and encouragement have been the guiding lights throughout this journey. Your love, sacrifices, and belief in my abilities have fuelled my determination to reach this milestone. This thesis is a testament to your endless faith in me.

ABSTRACT

This detailed study explores the complex information of ER5356 Aluminium alloy wall manufactured via Wire Arc Additive Manufacturing (WAAM) process. By comparing the findings with existing literature, the importance of precise control over process parameters for optimizing both alloy performance and additive manufacturing practices was highlighted. This investigation includes a complex metallographic analysis which begins with an in-depth examination of the microstructure. The metallographic preparation was done by deploying Weck's reagent, Pulton's reagents and Keller's reagent as an etchant and the efforts led to successful microstructure examination by achieving crystal-clear insights into grain structures of the specimens. Also EDS analysis and EBSD analysis was used to measure phase compositions and the average grain size of different regions from the wall. Mechanical property evaluation was performed including Vickers hardness testing and tensile testing to understand the performance of WAAM Al alloy samples. WAAM Al alloy samples were further subjected to High pressure torsion and analyzed further to understand the effect of severe plastic deformation of HPT on WAAM Al alloys. Corrosion resistance was examined closely through nitric acid mass loss test and potentiodynamic polarization tests, shedding light on the effect of beta phase content. This research expanded understanding of ER5356 alloy behavior in the WAAM context, providing valuable insights for the future of additive manufacturing and the potential applications of this alloy across diverse industries.

Table of Contents

Certificate of Declaration	iii
Acknowledgement	iv
Dedication	v
Abstract	vi
Table of Contents	vii
List of Figures	ix
List of Tables	xiii
Acronyms	xiv
Chapter 1: Introduction.....	1
1.1 Wire Arc Additive Manufacturing	1
1.2 Cold Metal Transfer	2
1.3 Aluminium and its alloys	4
1.4 Aluminium-Magnesium alloys	5
1.5 5xxx Series Aluminium alloys	6
1.6 Segregation in Al-Mg alloys	8
1.7 Precipitation in Al-Mg alloys	8
Chapter 2: Literature Review	9
2.1 Optimization of WAAM Parameters	9
2.2 Microstructure of WAAM Al alloys	11
2.3 Hardness of WAAM Al alloys	16
2.4 Tensile Test study	18
2.5 Effect of Mg loss on mechanical properties	20
2.6 Beta phase formation	22
2.7 High pressure torsion	25
2.8 Corrosion of Aluminium alloys	26
2.9 Effect of alloying on corrosion behavior	27

2.10 Corrosion study of ER5356 alloy	28
Chapter 3: Finding and insights from the literature.....	31
Chapter 4: Objectives.....	33
Chapter 5: Experimental work.....	34
5.1 Microstructural Characterization	34
5.2 Metallographic sample preparation	34
5.3 Characterization techniques	37
5.4 Mechanical Testing	39
5.5 Corrosion Testing	40
Chapter 6: Results and Discussions.....	42
6.1 Optical Microscopy study of WAAM ER5356	42
6.2 Sem study of WAAM ER5356	43
6.3 EDS Analysis	44
6.4 XRD Analysis	47
6.5 Hardness Analysis	47
6.6 Tensile Test Analysis	49
6.7 Heat Treatment	50
6.8 High Pressure Torsion	51
6.9 Corrosion Test Analysis	53
Chapter 7: Conclusion.....	62
7.1 Conclusions	62
7.2 Scope of Future Work	64
References.....	65

List of Figures

Figure 1.1: Chart illustrating the unit cost compared to quantity for traditional versus additive manufacturing methods.....	1
Figure 1.2: Common categorization of WAAM.....	2
Figure1.3: Describes the CMT cycle.....	3
Figure 1.4 Common shortcomings observed in objects manufactured using the WAAM method.....	3
Figure 1.5: Typical imperfections often found in an Aluminium alloy components fabricated using the WAAM technique.....	4
Figure 1.6: Binary phase diagram of Al-Mg alloy.....	6
Figure 2.1: Factors influencing the quality of WAAM products.....	10
Figure 2.2: Setup of WAAM with CMT [3].....	10
Figure 2.3: Sample of Wall made by CMT [3].....	10
Figure 2.4: Optical microstructure of different sections [5].....	11
Figure 2.5: Optical microstructure of interlayers [5].....	12
Figure 2.6: Optical microstructures of inter-layer region (c) and inner-layer region.....	13
Figure 2.7: Grain size data statics [5].....	14
Figure 2.8: Optical micrographs and statistical charts depicting grain size measurements conducted using Image-Pro Plus software [6].....	14
Figure 2.9: Schematic of Grain Growth [5].....	15
Figure 2.10: Hardness Distribution [5].....	16
Figure 2.11: Hardness Distribution [17].....	16
Figure 2.12: Tensile Test Sample and their Size as Per ASTM E8 Standards [9]..	18
Figure 2.13: Tensile test graph [19].....	20
Figure 2.14: Hardness test results for sample [19].....	21
Figure 2.15: XRD graphs from different journals [5] [8].....	22
Figure 2.16: XRD graph [9].....	23
Figure 2.17: SEM image of sample [9].....	24

Figure 2.18: Transmission Electron Microscope (TEM) images of ER5356 samples produced by WAAM (a) in the direction parallel to the travel path, and (b) in the direction perpendicular to the travel path [9].....	25
Figure 2.19: Diagram illustrating the HPT machine featuring the uniaxial compression stage (I) followed by the simultaneous torsion and compression stage (II) [46].....	26
Figure 2.20: Theoretical realms encompassing corrosion, passivation, and immunity of Aluminium at a temperature of 25°C have been investigated, as depicted in the relevant study [42].....	27
Figure 2.21: Schematic of Wall and Substrate [66].....	30
Figure 2.22: potentiostat dynamic plot [66].....	30
Figure 5.1: Wall manufactured by WAAM.....	34
Figure 5.2: Cut sample & FOSTEX FDK 7735 wire cutting EDM machine.....	34
Figure 5.1: Mounted samples.....	35
Figure 5.4: Grinding Operation.....	35
Figure 5.5 MetCo Bainpol Grinding/Polishing Machine	35
Figure 5.6: Polishing the Sample.....	36
Figure 5.6: Polishing the Sample.....	36
Figure 5.7: Etchants for Etching.....	37
Figure 5.8: Zeiss Axiovert A1 inverted microscope.....	37
Figure 5.9: Field emission scanning electron microscope.....	37
Figure 5.10: FE-SEM image of ER5356 sample.....	38
Figure 5.11: EDS image of ER5356 sample.....	38
Figure 5.12: PANalytical XRD machine.....	38
Figure 5.13: Hardness testing machine and samples.....	39
Figure 5.14: Tensile test specimens before testing.....	39
Figure 5.15: Tensile test specimens after testing.....	39
Figure 5.16: Immersed samples in nitric acid.....	40

Figure 5.17: Potentiodynamic polarization corrosion test setup.....	41
Figure 6.1: Optical microstructure of top area sample.....	42
Figure 6.2: (a) columnar grains, (b) Inter layer.....	42
Figure 6.3: optical microstructure of Keller’s etched specimen.....	43
Figure 6.4: Pulton’s Etchant (a)EDS & (b)SEM images.....	43
Figure 6.5: SEM and EDS Spectrum for Pulton’s & Weck’s Etchant.....	44
Figure 6.6: EDS layered image of non-etched sample.....	44
Figure 6.7: EDS mapping of non-etched sample.....	45
Figure 6.8: EDS point spectrum of non-etched sample.....	45
Figure 6.9: EBSD maps of a) top region b) middle region and c) bottom region of the wall along with their corresponding grain size distribution plot.....	46
Figure 6.10: a) Normal XRD scan b) Slow XRD scan of same sample.....	47
Figure 6.11: Hardness graph of different regions.....	48
Figure 6.12: Hardness graph of different regions.....	48
Figure 6.13: Stress strain curve a) for as deposited samples b) for solutionized samples.....	50
Figure 6.14: Solution heat treatment cycle.....	50
Figure 6.15: Dimensions of disk before and after HPT.....	51
Figure 6.16: Microhardness measurement from centre to edge of HPT sample...	51
Figure 6.17: Microhardness of top area HPT sample.....	52
Figure 6.18: Microhardness comparison of top area HPT sample.....	52
Figure 6.19: EBSD maps of a) top region b) middle region and c) bottom region of the wall along with their corresponding grain size distribution plot, (a1) top region (b1) middle region and (c1) bottom region also (d) shows the microstructure of as- deposited sample.....	54
Figure 6.20: EBSD maps of middle region of the wall a) As-deposited b) after solutionizing c) after ageing heat treatments with their corresponding grain size distribution plot, (a1) as deposited (b1) solutionized (c1) aged.....	55
Figure 6.21: NAMLT test readings from different regions of the wall.....	57

Figure 6.22: Represents the digital images of the middle region sample from a) as deposited b) as deposited after the immersion c) solutionized after the immersion d) aged after the immersion for 24hrs in nitric acid..... 58

Figure 6.23: Tafel plots of a) As- deposited b) solutionized and c) Aged samples 60

Figure 6.24: FE-SEM images of a) As-deposited b) solutionized c) aged samples of middle region and a1), b1) and c1) shows digital images of the same samples; also, a2), b2), and c2) show the FE-SEM images of the corresponding samples, respectively..... 62

List of Tables

Table 1.1: Aluminium alloy families.....	5
Table 1.2: Elemental composition of ER5356 alloy	7
Table 2.1: Optimized parameters of WAAM.....	9
Table 2.2: Range of stress & elongation from various literature sources	19
Table 2.3: Chemical composition of alloy.....	23
Table 2.4: Parameters of corrosion according to potentiostat tests	30
Table 6.1: Data for measured hardness values	48
Table 6.2: Stress strain data table from test results	49
Table 6.3: Test data for NAMLT test.....	56
Table 6.4: Corrosion rate of different samples.....	58

Acronyms

1. AM - Additive Manufacturing
2. CAD - Computer-Aided Design
3. CNC - Computer Numerical Control
4. WAAM - Wire Arc Additive Manufacturing
5. CMT - Cold Metal Transfer
6. GMAW - Gas Metal Arc Welding
7. IGC - Intergranular Corrosion
8. SCC - Stress Corrosion Cracking
9. SSS α - Supersaturated Solid Solution of Mg in the Aluminium Matrix
10. TEM - Transmission Electron Microscopy
11. WFS - Wire Feed Speed
12. TS – Travel Speed
13. TS - Tensile Strength
14. HV - Vickers Hardness
15. FCC - Face-Centered Cubic
16. UTS - Ultimate Tensile Strength
17. YS - Yield Strength
18. EL - Elongation
19. XRD - X-ray Diffraction
20. SEM - Scanning Electron Microscopy
21. EDS - Energy-Dispersive X-ray Spectroscopy
22. HPT - High-Pressure Torsion
23. EDM - Electric Discharge Machining
24. FE-SEM - Field Emission Scanning Electron Microscope
25. NAMLT - Nitric Acid Mass Loss Test
26. PDP - Potentiodynamic Polarization

Chapter 1

Introduction

Additive Manufacturing (AM) is an engineering technique that builds objects layer by layer through deposition of material. Over the past 30 years, AM methods have seen significant development, with increasing recognition of their potential each year. Initially used for rapidly creating plastic prototypes directly from CAD models, simplifying product development, recent focus in AM research has shifted towards fabricating complex metal components. In this domain, AM offers numerous advantages over traditional subtractive methods like CNC machining. Firstly, it allows for the manufacture of intricate components that would be challenging or even impossible to produce using subtractive techniques. Additionally, AM reduces material waste thanks to its geometrical precision. In general, the benefits of AM are more pronounced for smaller production quantities, in contrast to conventional manufacturing techniques the cost per unit decreases.

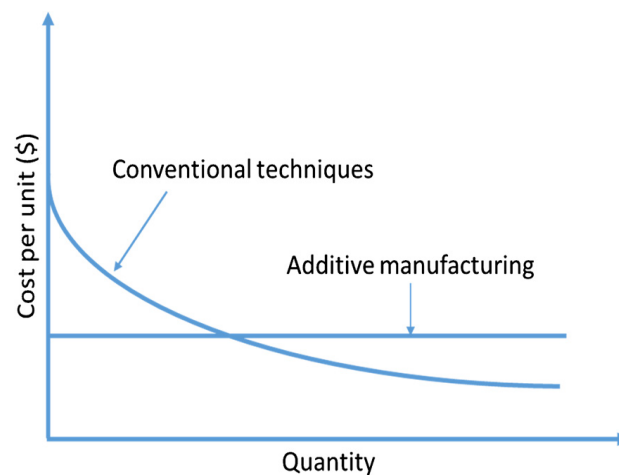


Figure 1.1: Chart illustrating the unit cost compared to quantity for traditional versus additive manufacturing methods

1.1 Wire and Arc Additive Manufacturing

The methodology selected for this project is Wire and Arc Additive Manufacturing (WAAM). Through the use of an electric arc, WAAM melts wires electrically. As the wire liquefies, it is extruded in bead form along a predetermined path by either a robot or CNC machine. These beads fuse together to form a layer, and so on until the component is completely produced. The surface upon which these layers are constructed is referred to as the substrate, which can either remain integral to the final component or be removed post-WAAM processing. The selection of an appropriate substrate is paramount, taking into account considerations such as part dimensions and building orientations.

WAAM is well-suited for manufacturing complex components with strong structural reliability across a variety of materials. It has the potential to reduce lead times, bottom manufacturing costs, and minimize wastage of material compared to conventional subtractive manufacturing methods. However, WAAM does have some limitations. While it offers less design freedom compared to other additive manufacturing techniques, careful attention to build orientation, sequence, and process design constraints is necessary. The rough surface finish and high heat input resulting often require post-processing, which adds another layer of consideration. Nonetheless, it's important to recognize that WAAM presents a wide range of design opportunities simultaneously.

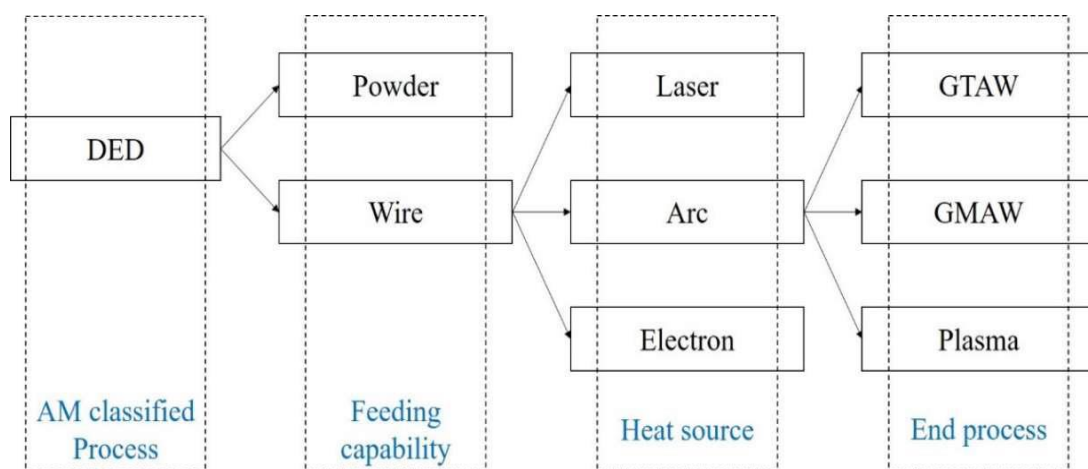


Figure 1.2: Common categorization of WAAM

1.2 Cold metal transfer

Cold Metal Transfer (CMT) stands as a modified version of gas metal arc welding (GMAW), uniquely advantageous for Wire and Arc Additive Manufacturing (WAAM) due to its combination of elevated deposition rates and minimal heat input. Within CMT, welding parameters like current, voltage, and wire feed are concurrently regulated. Figure 1.3 illustrates the distinct phases of the CMT cycle.

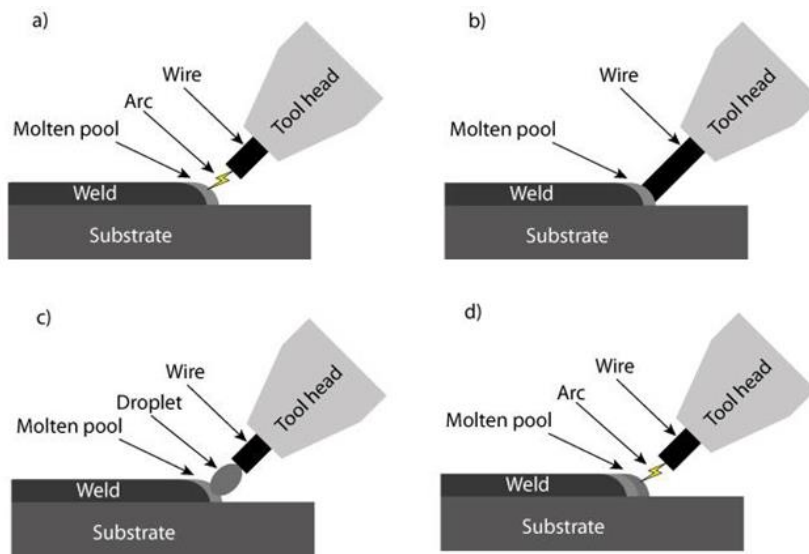


Figure 1.3: Describes the CMT cycle. a) The wire approaches the material and an arc occurs. b) The wire is pushed in to the molten pool and the arc is put out. c) The wire is retracted, and droplet is formed and released on the weld pool. d) The cycle repeats

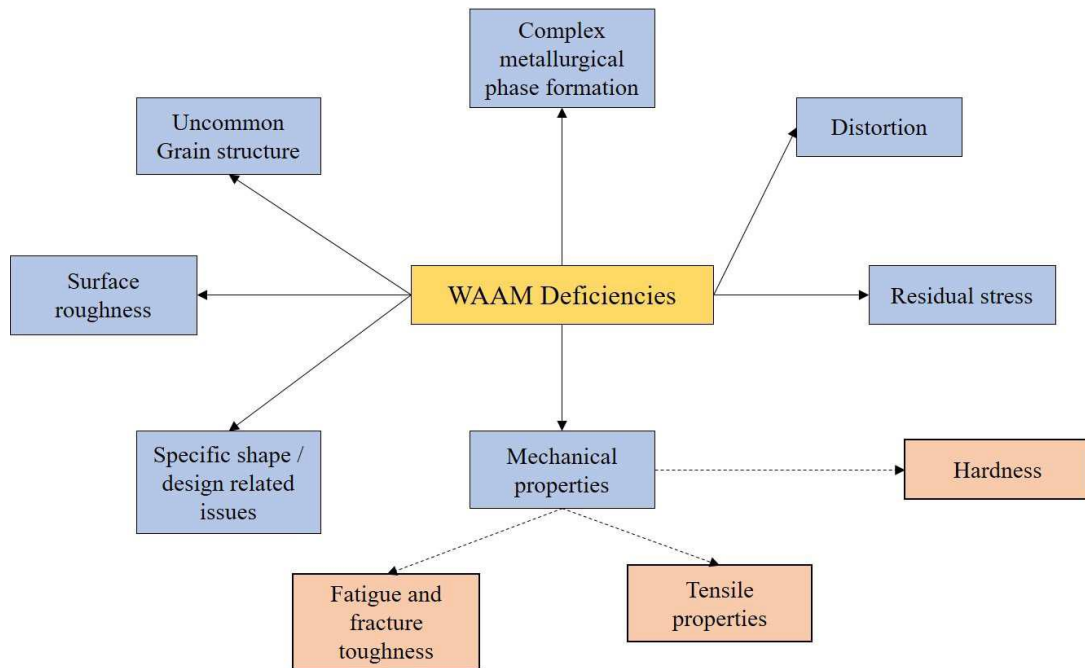


Figure 1.4: Common shortcomings observed in objects manufactured using the WAAM method

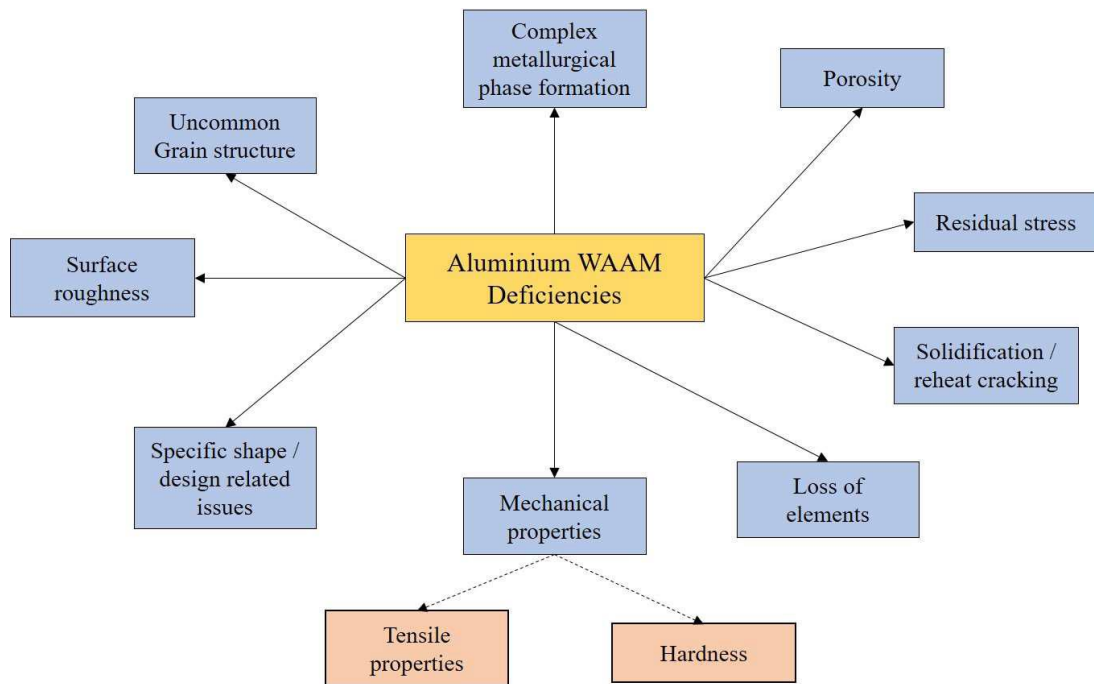


Figure 1.5: Typical imperfections often found in an Aluminium alloy components fabricated using the WAAM technique

1.2 Aluminium and its alloys

1.3.1 Properties of Aluminium

Aluminium, reigns as the most widely utilized non-ferrous metal, finding applications across a broad spectrum of fields such as construction, transportation, packaging, and more. Its unique blend of properties makes Aluminium exceptionally attractive and cost-effective.

One notable characteristic of Aluminium is its lightweight nature, having a density of 2698.8 kg/m³, nearly one-third that of iron (7850 kg/m³), which makes it invaluable in air, sea and land transportation sectors. Furthermore, Aluminium's remarkable resistance to corrosion in the majority of conditions because of the quick development of an Al₂O₃ protective oxide film. Its superb formability is another standout feature, stemming from its excellent ductility, malleability, and impressive joining properties, alongside its forgeability. Lastly, Aluminium's low melting point of 660°C enhances its exceptional casting properties

The adaptability of Aluminium and its alloys across a wide range of industries is demonstrated by the several forms in which they are made and generally categorized as standard goods. These forms include plate, sheet, rod, tube, pipe etc.

1.3.2 Classification of Aluminium Alloys

In terms of engineering processes, Aluminium alloys can be divided into two primary groups as outlined in references [1, 2, 8]:

- (a) Cast Alloys: Produced by pouring molten Aluminium metal into a mold.
- (b) Wrought Alloys: Alloys that undergo different types of mechanical shaping, including both hot and cold working, without reaching a molten state.

1.3.3 Aluminium Alloy Families

Aluminium Alloy Series		
Series number	Alloying element	Alloy Features
1XXX	ALUMINIUM	Electrically conductive
2XXX	COPPER	Increased strength
3XXX	MANGANESE	Food safe
4XXX	SILICON	Bottom melting point
5XXX	MAGNESIUM	Higher corrosion resistance
6XXX	MAGNESIUM & SILICON	Respond well to heat treatment
7XXX	ZINC	High strength

Table 1.1: [source: Deco Ultra Australia]

1.4 Aluminium-Magnesium Alloys

Aluminium-Magnesium alloys, part of the 5xxx series of Aluminium alloys, primarily enhance their strength through strain hardening rather than heat treatment, commonly utilizing cold working during fabrication. Magnesium content in these alloys ranges from 3 to 13 weight percent, and the inclusion of elements like Mn and Cr can increase their resistance to stress corrosion cracking. In Figure 1.6, the binary Aluminium-Magnesium equilibrium phase diagram is depicted. This diagram illustrates the existence of the phase (Aluminium solid solution) and the β phase (Al_3Mg_2) in Aluminium alloys.

The solubility of Magnesium is decreases with decreasing temperature in the Aluminium matrix. At the eutectic temperature ($450^\circ C$), the solid solution holds the maximum Mg content, reaching 15.35 wt. %. However, the solubility of Magnesium in the solid solution drops to around 2 weight percent at $100^\circ C$. The β phase forms as a result of this decrease in solubility, which is altered by exposure to high temperatures as well as cold working. It is expected that the precipitation process will start at the boundaries of the grains, move on to the dislocations, and finally spread throughout the matrix.

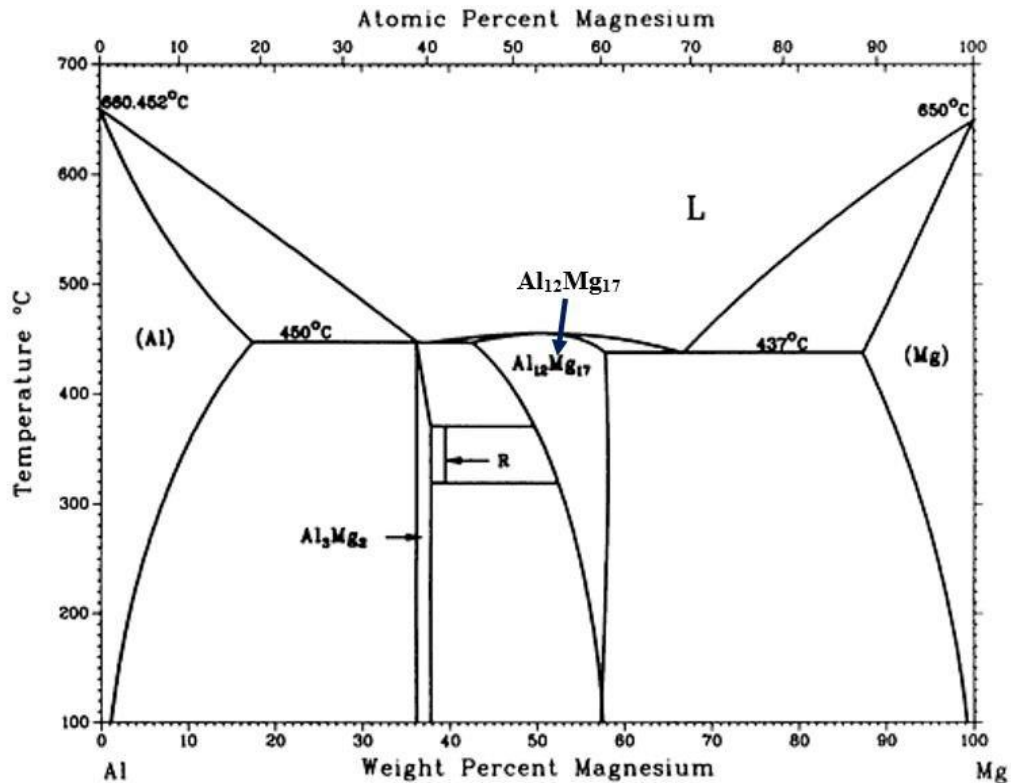


Figure 1.6: Binary phase diagram of Al-Mg alloy

1.5 5xxx Series Aluminium alloy

Magnesium is the key alloying element in the 5xxx series alloys. When Magnesium is utilized either alone or with addition of manganese, it produces an alloy with moderate to high strength that is capable of undergoing work hardening. Magnesium proves notably more effective than manganese as a strengthening agent, with approximately 1.25% Mn equating to 0.80% Mg, and it can be incorporated in larger quantities. Alloys within this series demonstrate favourable welding properties and resistance to corrosion in marine environments. Nevertheless, it is imperative to restrict the extent of cold working and adhere to safe operating temperatures, particularly for alloys with higher Magnesium content (exceeding ~3.55% for operating temperatures surpassing ~70°C), to mitigate susceptibility to stress-corrosion cracking.

1.5.1 ER5356 Aluminium alloy

ER5356 is a high-performance Aluminium welding alloy that belongs to 5xxx series of Aluminium alloys. This particular alloy is highly regarded in the world of welding due to its exceptional properties and wide-ranging applications. ER5356's composition, welding characteristics, and specific applications make it a top choice for professionals across various industries.

ER5356 has a nominal composition (wt.-%) of 5% Magnesium, with the remainder being Aluminium. It has emerged as the most widely used filler alloy due to its compatibility with most base alloys, its robust strength, and its excellent feedability when utilized as a Gas Metal Arc Welding (GMAW) electrode wire. Typical applications for ER5356 include ships, pressure vessels, bicycles, truck and automotive parts. However, this filler metal does have a significant limitation: it is unsuitable for service temperatures exceeding above 70°C. This is attributed to the formation of Al₃Mg₂ at higher temperatures along the grain boundaries, rendering the alloy susceptible to stress corrosion.

Composition:

The elemental composition of Aluminium 5356 alloy is outlined in the following table.

Element	Content (%)
Aluminium, Al	92.9-95.3
Magnesium, Mg	4.50-5.50
Iron, Fe	0.40
Silicon, Si	0.25
Copper, Cu	0.10
Zinc, Zn	0.10
Titanium, Ti	0.060-0.20
Chromium, Cr	0.050-0.20
Manganese, Mn	0.050-0.20
Beryllium, Be	0.000800
Other, total	0.15
Other, each	0.050

Table 1.2: [Source: Research Gate]

1.6 Segregation in Al-Mg Alloys

Earlier research has indicated that Magnesium tends to accumulate at both grain boundaries and the exposed surface of Aluminium [9, 23, 24]. Vetrano et al. [9] noted a rise in Magnesium levels at grain boundaries in samples aged at 175°C for 100 hours, with a ratio of Magnesium concentration at grain boundaries to that in the matrix being 2.5:1. This segregation notably impacts local electrochemical characteristics and bears implications for properties relevant to service, such as stress corrosion cracking (SCC) and intergranular corrosion (IGC) [23].

1.7 Precipitation in Al-Mg Alloys

In the 5xxx series of Aluminium alloys, the sequence of precipitation has been investigated and observed to follow the following order:

SSS α (supersaturated solid solution of Mg in Al alloy matrix) \rightarrow GP zones $\rightarrow \beta'' \rightarrow \beta' \rightarrow \beta$

During the initial phase of thermal exposure, GP zones, characterized by one or two atom planes formed between the grain boundary and the grain itself, are detected [19, 32]. These zones subsequently transform into β'' particles (Al_3Mg) [31]. As thermal exposure continues, GP zones and β'' particles dissolve, leading to the precipitation of β' at grain boundaries. However, despite the detection of numerous defects using techniques like transmission electron microscopy (TEM) and differential scanning calorimetry (DSC), Starink et al. [31] did not find any evidence of β' on defects such as dislocation loops.

At temperatures above 200°C, the stable continuous equilibrium β phase is observed, which has an FCC structure with a lattice parameter of 2.284 nm and 1168 atoms per unit cell. The final composition of the β phase is Al_3Mg_2 . It is well known that precipitation is a temperature and time-dependent process, occurring more rapidly at higher temperatures. The structure of grain boundaries, characterized by higher free energy than the matrix, provides preferential sites for the precipitation process due to their disturbed nature and high free volume.

Chapter 2

Literature Review

Wire Arc Additive Manufacturing (WAAM) is emerging as one of the most prominent manufacturing processes in recent years. WAAM enables the production with high deposition rates and is applicable to many alloys like stainless steel, copper, Aluminium, and titanium alloys. Aluminium alloy, known for its excellent low density, superior corrosion resistance and fatigue properties and has found widespread use in automotive and aerospace applications, making the application of WAAM in Al components significant.

Several studies have explored the fabrication of Aluminium alloy components using WAAM and have investigated their metallurgical and mechanical properties. Porosity and oxidation are common challenges in WAAM of Aluminium alloys. A decrease in porosity with increased current, leading to improved mechanical properties.

2.1 Optimization of WAAM Parameters

Optimizing the parameters in Wire Arc Additive Manufacturing (WAAM) processes is a crucial process for attaining superior material properties and overall performance. This optimization process involves a systematic adjustment of key parameters such as voltage, current, work feed speed, tip to work distance and travel speed. The objective is to strike a delicate balance that ensures the optimal deposition of material while minimizing inherent challenges like porosity, anisotropy, and oxidation.

The attached data table, compiled from a variety of authoritative sources, provides a broad overview of optimized parameters resulting from extensive research efforts.

Table 2.1: Optimized parameters of WAAM

S.No	Travel Speed mm/sec	Work Feed Speed m/min	Tip to Work Distance mm	Waiting Time sec	Argon Lit/min	Current Amp	Voltage Volt	Ref.
1	5					110	17	[22]
2	4					110	18	[22]
3	10	6	18	30	25	140-150	18-20	[5]
4	5	1.4	5	300		100		[7]
5	3.33	6			15	160		[11]
6	5.33	6			15	160		[11]
7	8.33	6			15	160		[11]
8	10	8	10+3	30	14	92	16	[12]
9	10	8	10+3	60	14	92	16	[12]
10	10	8	10+3	120	14	92	16	[12]
11	12.66	10	10+3	30	14	92	16	[12]
12	12.66	10	10+3	60	14	92	16	[12]
13	12.66	10	10+3	120	14	92	16	[12]
14	10	8	10		14	91-92	15.5	[13]
15	5.33	0.7	5		12	90	14-18	[14]
16	5.33	0.7	5		12	105	14-18	[14]
17	10	7.5			20	168	16.9	[15]
18	5		13	300	12	100	17+2	[16]
19	4				14	220-290	24	[18]

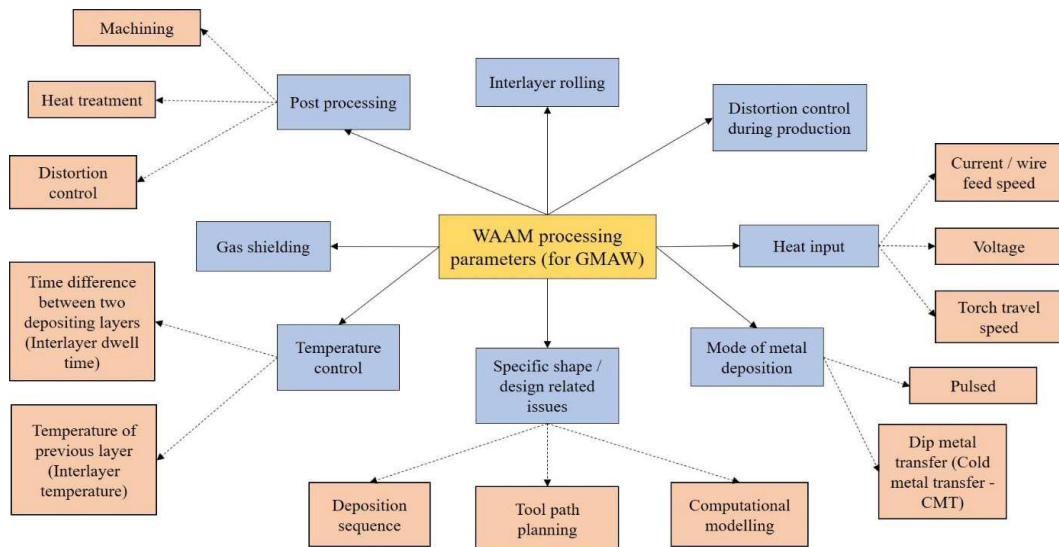


Figure 2.1: Factors influencing the quality of WAAM products

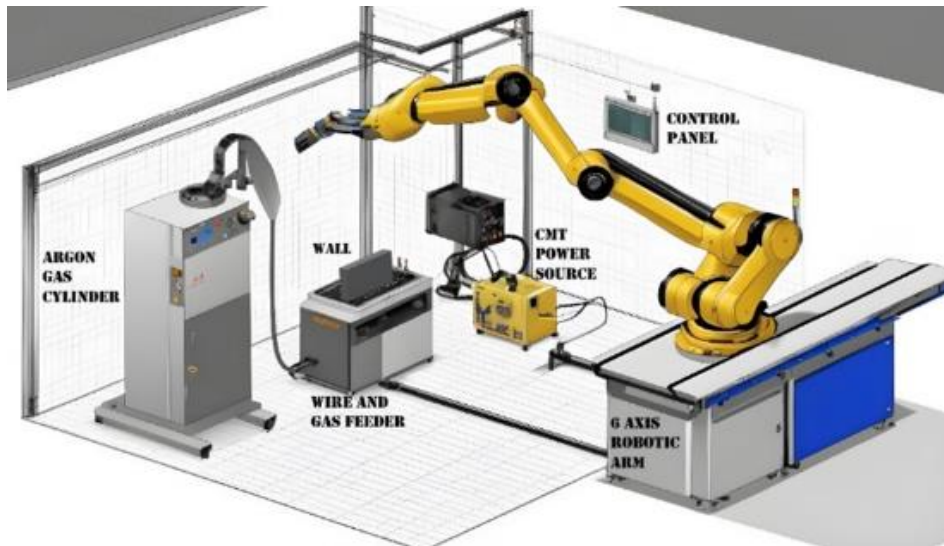


Figure 2.2: Setup of WAAM with CMT [3]

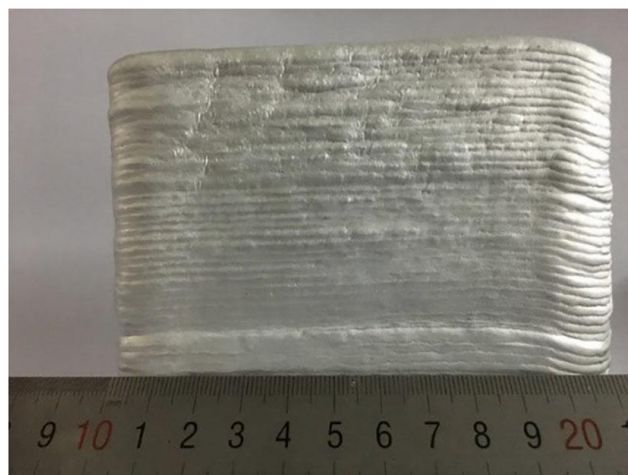


Figure 2.3: Sample of Wall made by CMT [3]

2.2 Microstructure of WAAM Al Alloys

The microstructure of the ER5356 component exhibits distinct characteristics within different regions. Figure 2.4 below illustrate the inner layer, interlayer, and microstructures of the component.

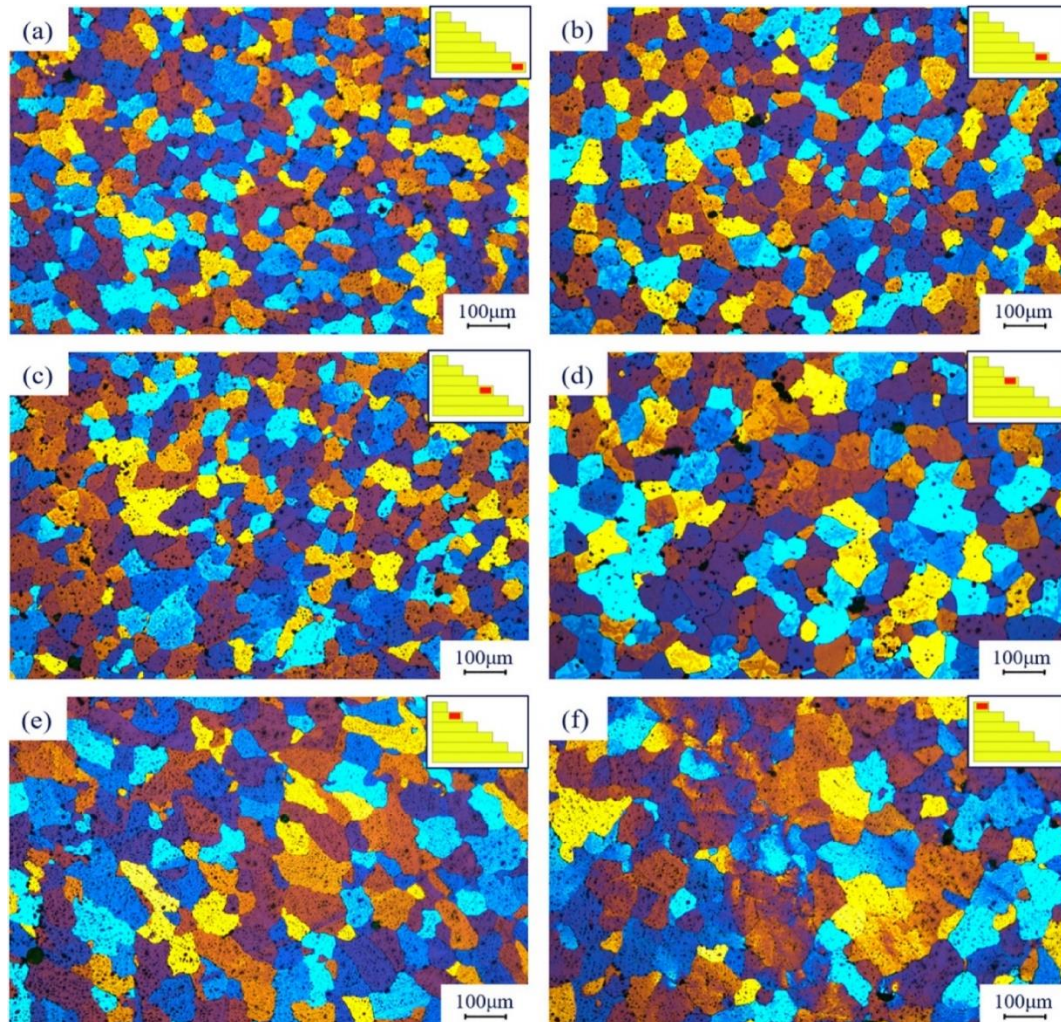


Figure 2.4: Optical microstructure of different sections [5]

In Figure 2.4, as reported by Wang et al. [5], the bottom region microstructure is primarily contains equiaxed grains with small diameters. Progressing towards the middle region, some columnar grains are also visible, while the size of equiaxed grains become larger compared to the bottom region. However, the most notable difference is observed in the top region, where grains are substantially larger. In this area, equiaxed grains transform into columnar grains with clear directionality, signifying significant microstructural variations with deposition height.

Figure 2.5 Wang et al [5] provides a view of the interlayer, which is characterized by a strip-like region having very small equiaxed grains. Notably, interlayer region contains lots of pores, showing poor mechanical properties compared to the inner layer region. Additionally, the morphology of the interlayer exhibits variations, with some regions appearing flat and others curved. These variations are attributed to the perpendicular filling paths of adjacent deposited layers.

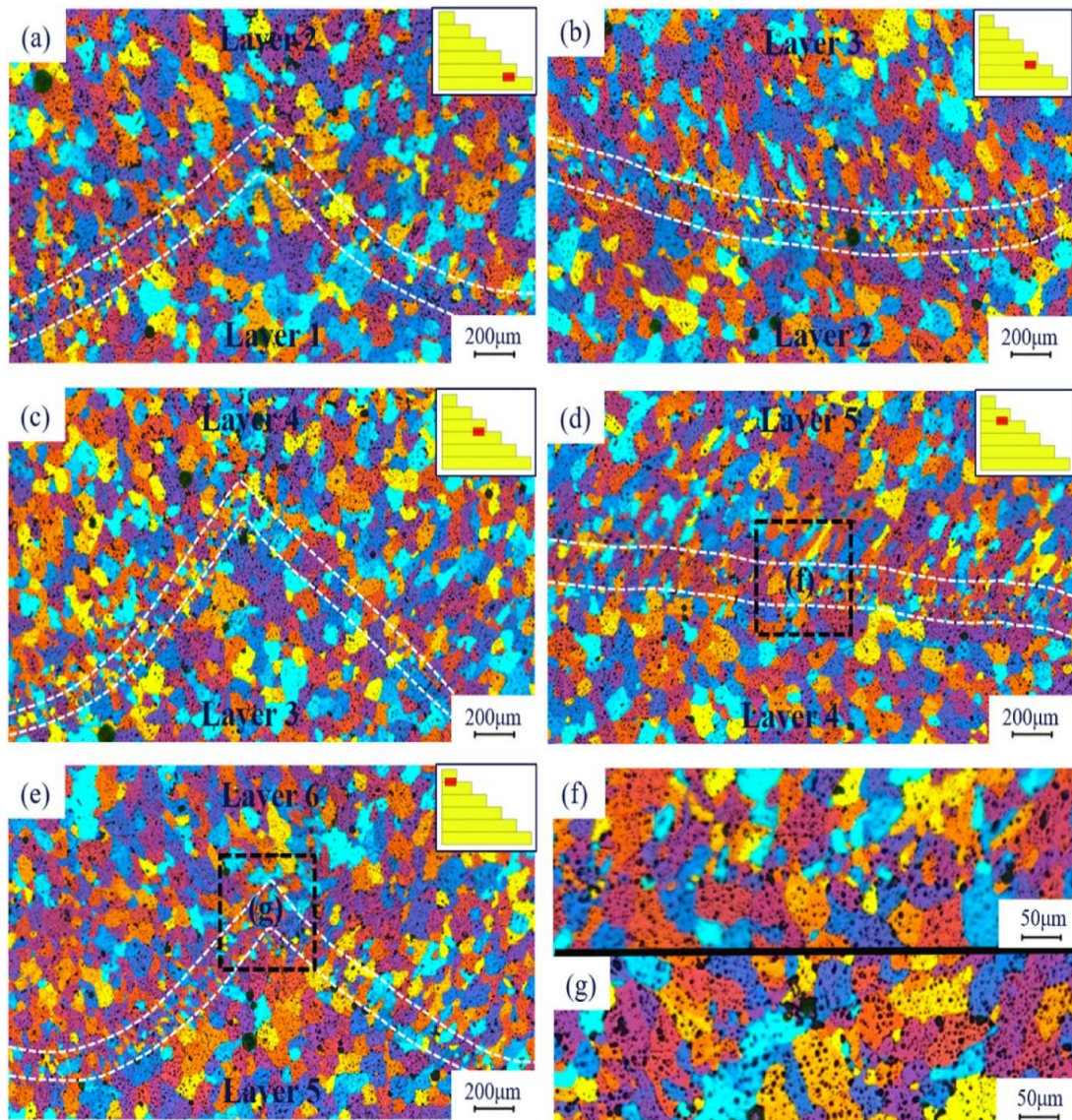


Figure 2.5: Optical microstructure of interlayers [5]

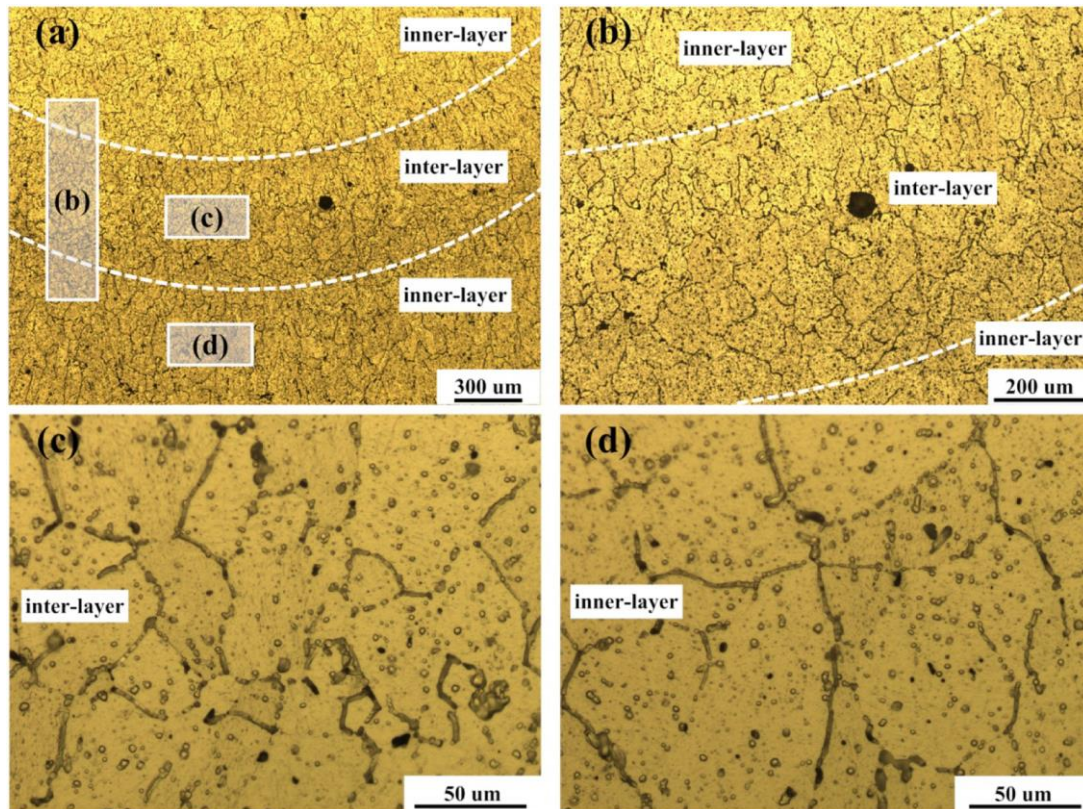


Figure 2.6: Optical microstructures of inter-layer region (c) and inner-layer region [6]

2.2.1 Microstructural Features

In the interlayer under specific conditions as studied by Su et al. [6] (with a travel speed of 0.6 m/min and a wire feed speed of 8.0 m/min), the microstructure is primarily composed of smaller equiaxed grains and fine columnar grains with nonuniform characteristics. On the other hand, the interlayer under the same circumstances primarily shows coarse equiaxed grains, with a small amount of elongated coarse columnar grains near the interlayer's boundary. This variation in microstructure across different regions highlights the impact of process parameters on grain formation.

To gain a deeper understanding of the changes in grain size during the WAAM process, statistical grain size data in Figure 2.6 reveal significant trends. Su et al. [6] found that with increasing deposition height the maximum grain size progressively increases from 160–170 μm to 200–210 μm , whereas the average grain size increases from 85.27 μm to 113.28 μm . These shifts in grain size underscore the dynamic nature of microstructures during WAAM processing.

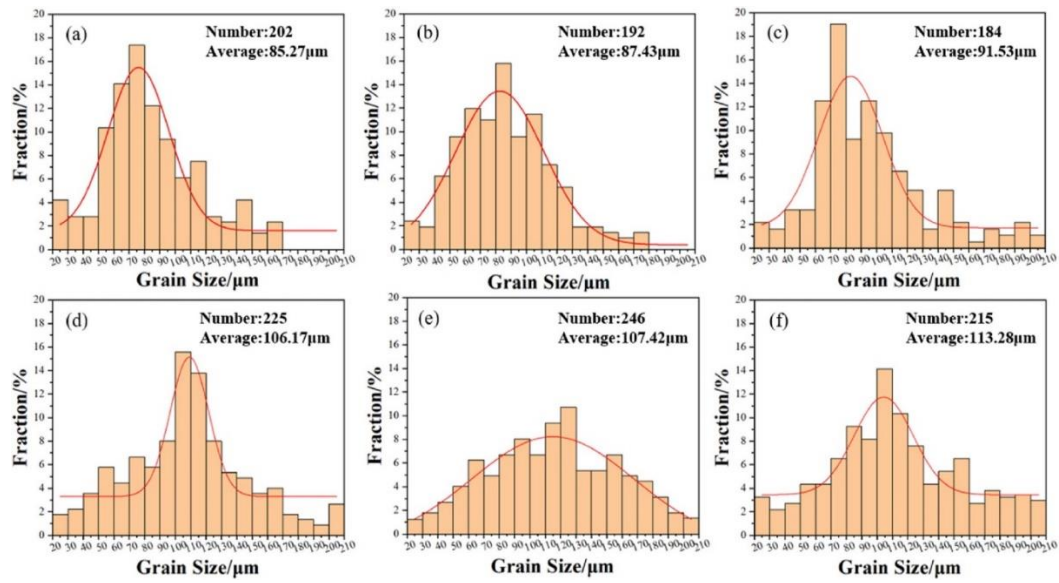


Figure 2.7: Grain size data statics [5]

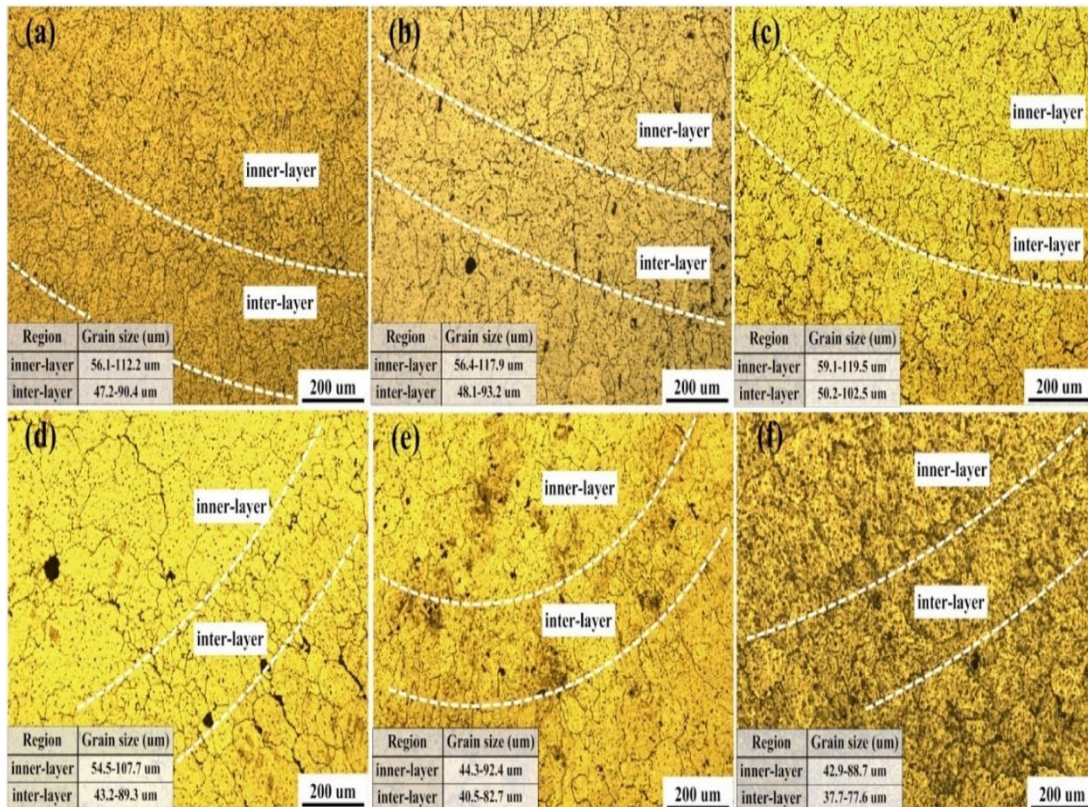


Figure 2.8: Optical micrographs and statistical charts depicting grain size measurements conducted using Image-Pro Plus software [6]

2.2.2 Microstructure variations

Microstructural variation arises due to the thermal cycling and accumulation of heat during the deposition of successive layers. Wang et al [5] reported that during the initial stages of WAAM, the preheated layer experiences significant heat absorption and dissipation due to the high-temperature arc. This process leads to nonuniform nucleation, resulting in the rapid growth of grains in various directions. The presence of multiple grain nuclei leads to competition among them. Subsequent layers introduce local thermal cycling, as heat is transferred to bottom layers, causing some grains to coarsen. This complex thermal environment promotes the growth of equiaxed and columnar grains at different stages of deposition.

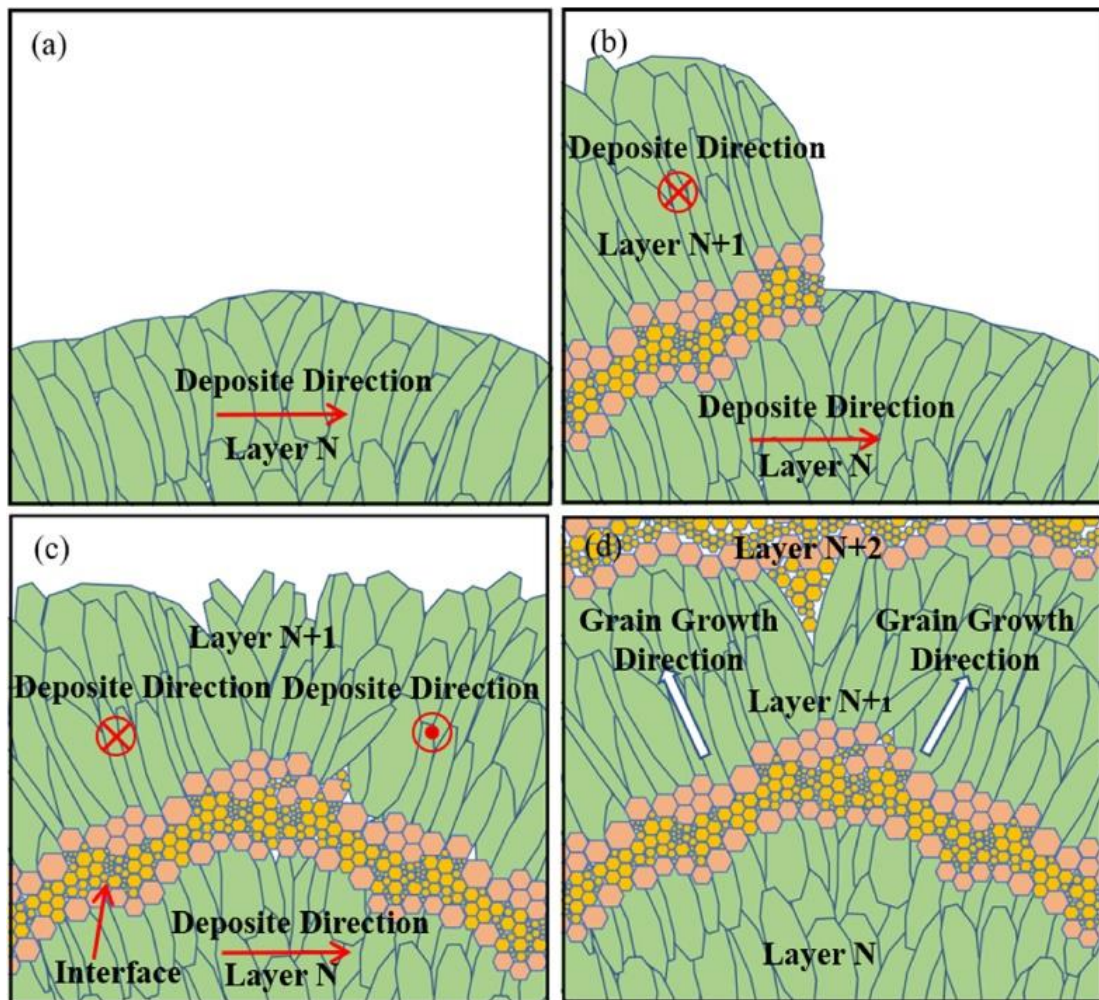


Figure 2.9: Schematic of Grain Growth [5]

2.3 Hardness of WAAM Al Alloys

The hardness of a material is a fundamental mechanical property that can provide valuable insights into its suitability for specific applications. In the context of Wire Arc Additive Manufacturing, understanding the hardness characteristics of the deposited material is essential for assessing its mechanical performance.

Assessing the microhardness of ER5356 Aluminium alloy components fabricated with Wire Arc Additive Manufacturing technology offers valuable insights into the material's mechanical characteristics. Fig. 2.10 presents a schematic diagram illustrating the microhardness distribution across these components.

According to Wang et al [5] the average microhardness value for the AA5356 thin-walled components is recorded at 73.9 HV (Vickers Hardness). This measurement offers a valuable reference point for understanding the material's resistance to plastic deformation and its suitability for specific applications.

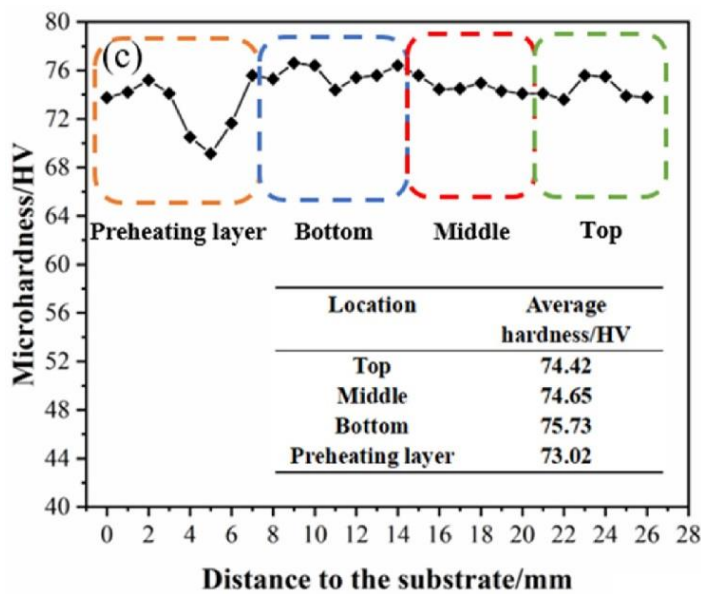
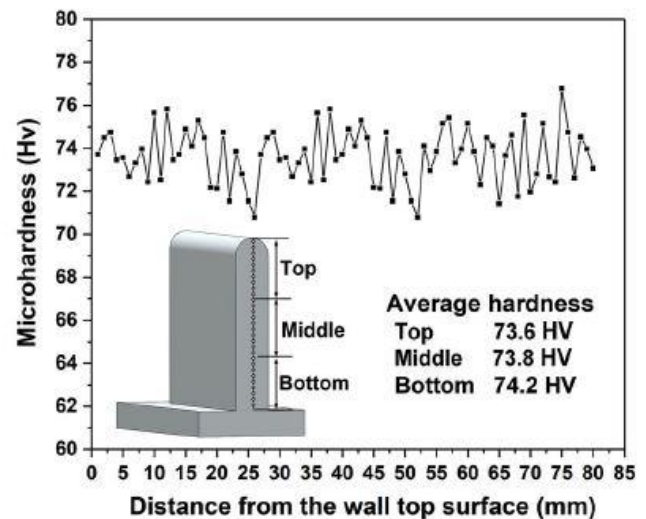


Figure 2.10: Hardness Distribution [5]

Figure 2.11: Hardness Distribution [17]



2.3.1 Regional Hardness Variations

The microhardness values exhibit variations across different regions of the component. Wang et al. [17] reveals that the average microhardness is highest in the bottom region, the top region exhibits the lowest microhardness while in the middle region is intermediate between them.

This regional variation in microhardness can be attributed to several factors:

1. **Grain Size:** In the bottom region, the microstructure consists of smaller equiaxed grains. Smaller grain sizes are often associated with higher hardness values. The reduced grain size contributes to the higher average hardness observed in this region.
2. **Heat Dissipation:** The bottom layer of the component is deposited directly on the base plate, allowing for efficient heat dissipation. Faster heat dissipation typically results in enhanced material hardness.
3. **Temperature Gradient:** The middle region, situated between the bottom and top layers, experiences a higher temperature gradient compared to the other regions. This thermal environment influences the material's mechanical properties, resulting in intermediate hardness values.
4. **Heat Dissipation at the Top:** In contrast, the top layer, being exposed to open air, experiences rapid heat dissipation. This phenomenon causes a reduction in microhardness compared to the middle and bottom regions.

2.3.2 Uniform Phase Structure

Despite the differences in microhardness across the top, middle, and bottom regions, all regions exhibit the same FCC (Face-Centered Cubic) phase structure. This consistency in phase structure suggests that variations in microhardness are primarily influenced by factors such as grain size and thermal effects rather than changes in material phase [17].

2.4 TENSILE TEST STUDY

The assessment of tensile properties is a fundamental aspect of material characterization, essential for determining the material's mechanical behavior under various loading conditions. This section delves into the tensile properties of the examined material, shedding light on its strength, yield behavior, and ductility.

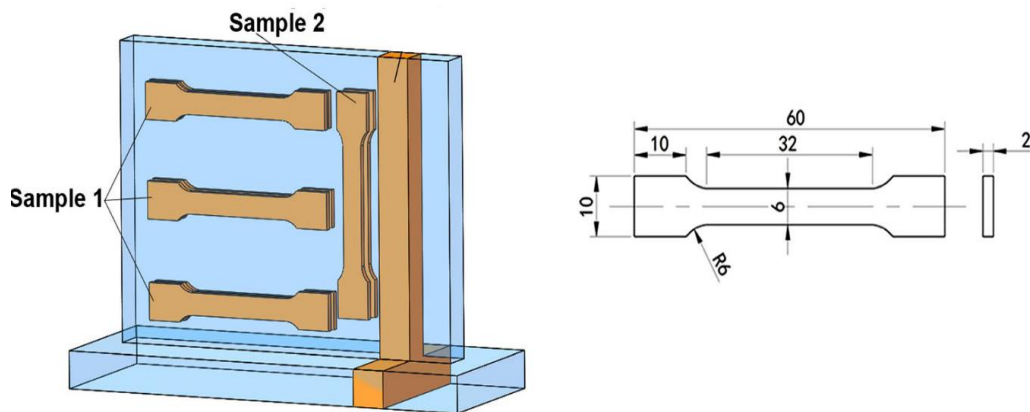


Figure 2.12: Tensile Test Sample and their Size as Per ASTM E8 Standards [9]

In the study of tensile properties, various test specimens were fabricated using 5356 Aluminium Magnesium alloy through the Wire Arc Additive Manufacturing process. The obtained tensile test results reveal notable variations in mechanical properties across different regions of the specimens.

In the top section of the samples, Wang et al. [17] noted a yield stress (YS) of 111 MPa, ultimate tensile stress (UTS) of 244.4 MPa, and an elongation (EL) of roughly 25.9%. Progressing to the middle portion, a slightly elevated a YS of 114.3 MPa, UTS of 263.6 MPa, and an EL of approximately 24.9% were observed. Conversely, the bottom segment displayed the highest UTS at 284.4 MPa, although with a slightly bottom EL of about 25.8% compared to the top and middle sections. This variance in tensile properties is attributed to differing heat dissipation conditions encountered by each segment during the manufacturing process, showcasing a compromise between strength and ductility.

Interestingly, the tensile strength of the longitudinal samples was marginally bottom than that of the transverse ones, potentially due to the presence of some pores and cracks between layers, as indicated by the test findings.

When comparing these outcomes with the characteristics of the as-cast 5356 Aluminium Magnesium alloy, it becomes evident that the WAAM process significantly enhances mechanical performance. According to Gao et al. [70], the as-cast alloy displayed a UTS of 202.4 MPa, a YS of 87.2 MPa, and an EL of 23.8%. In contrast, the WAAM specimens demonstrated an average increase in UTS and YS of about 19.8% and 22.5%, respectively, compared to the as-cast Aluminium alloy.

The table below shows the data collected from various literature sources to provide an overview of the range of stress and elongation values observed in previously made samples:

Table 2.2: Range of stress and elongation from various literature sources

S.No	UTS Mpa	YS Mpa	Elongation %	Loading Rate mm/min	position	Ref.
1	192.65			1	Horizontal	[22]
2	201.37			1	Horizontal	[22]
3	244.4	111	25.9	1	TOP	[5]
4	263.6	114.3	24.9	1	MIDDLE	[5]
5	284.4	116.1	25.8	1	BOTTOM	[5]
6	220	88.5	19.4	1	VERTICAL	[5]
7	267.6		33.9	1	HORIZONTAL	[7]
8	236.7		23.8	1	VERTICAL	[7]
9	212.6		20.69	1	HORIZONTAL	[11]
10	241.7		34.33	1	HORIZONTAL	[11]
11	245.6		35.28	1	HORIZONTAL	[11]
12	270	120	28	3.2	HORIZONTAL	[12]
13	269	120	21	3.2	HORIZONTAL	[12]
14	265	105	23	3.2	HORIZONTAL	[12]
15	275	120	22	3.2	HORIZONTAL	[12]
16	276	120	23	3.2	HORIZONTAL	[12]
17	270	121	22	3.2	HORIZONTAL	[12]
18	270	114	28.3	3.2	HORIZONTAL	[13]
19	254+-6	114+-2.7	17.1	3.2	VERTICAL	[13]
20	255.3		40	5	HORIZONTAL	[14]
21	166		16.3	5	VERTICAL	[14]
22	258		37	5	HORIZONTAL	[14]
23	160		18	5	VERTICAL	[14]
24	232.4		27.7	2	VERTICAL	[15]
25	265.8		47.8	2	HORIZONTAL	[15]
26	230	150	17	1	HORIZONTAL	[16]
27	276	125	30	1	HORIZONTAL	[16]

2.5 Effect of Mg Loss on Tensile and Hardness Properties of wall

This section focuses on examining the influence of Magnesium (Mg) loss on the tensile and hardness properties of the material.

In the study by Yuan et al. [19], two samples labeled as #1 and #6 were analyzed. Sample #1 was extracted from the top section of the wall and deposited using a 90A current, while sample #6 was deposited using a 110A current. These samples represent significant differences in Mg loss rates due to the varying heat rates during the deposition of the wall. Sample #1 displayed an Mg loss rate of 5.56%, while sample #6 exhibited a higher loss rate of 17.31%.

Anisotropy, or directional variation in material properties, is often observed in Welding Additive Manufacturing (WAAM) components due to fusion defects occurring more readily in the inter-layer zones. In general, the sample's tensile strength is higher in the horizontal direction than the vertical direction. Sampling was done from the WAAM component in a horizontal direction to reduce the impact of fusion defects on tensile strength.

As depicted in Figure 2.13, sample #1, characterized by a Magnesium loss rate of 5.56% and a current of 90 A, demonstrated a tensile strength of 255.4 MPa and an elongation of 26.5%. With an increase in current to 110 A and an associated Magnesium loss rate of 17.31%, While the elongation increased to 31.2%, the tensile strength dropped to 240.7 MPa. This suggests that a decrease in the amount of Magnesium present in Al-Mg alloys leads to a rise in ductility and a decrease in mechanical properties.

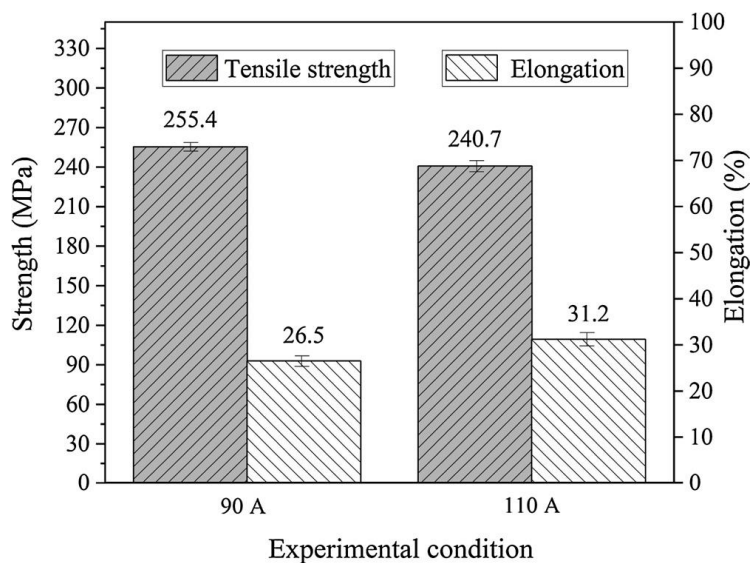


Figure 2.13: Tensile test graph [19]

In Figure 2.14, the hardness distribution across the cross-sections of samples #1 and #6 is depicted, indicating minimal disparities in hardness between the two samples. Nevertheless, the majority of testing points in sample #1 exhibited higher hardness values compared to those in sample #6. Specifically, the hardness of sample #1 measured at 71.50 HV, while sample #6 showed a slightly bottom average hardness of 67.64 HV. The observed reduction in hardness of 5.7% corresponds to the increase in Magnesium loss rate from 5.56% to 17.31%, which aligns with the results obtained from the tensile tests.

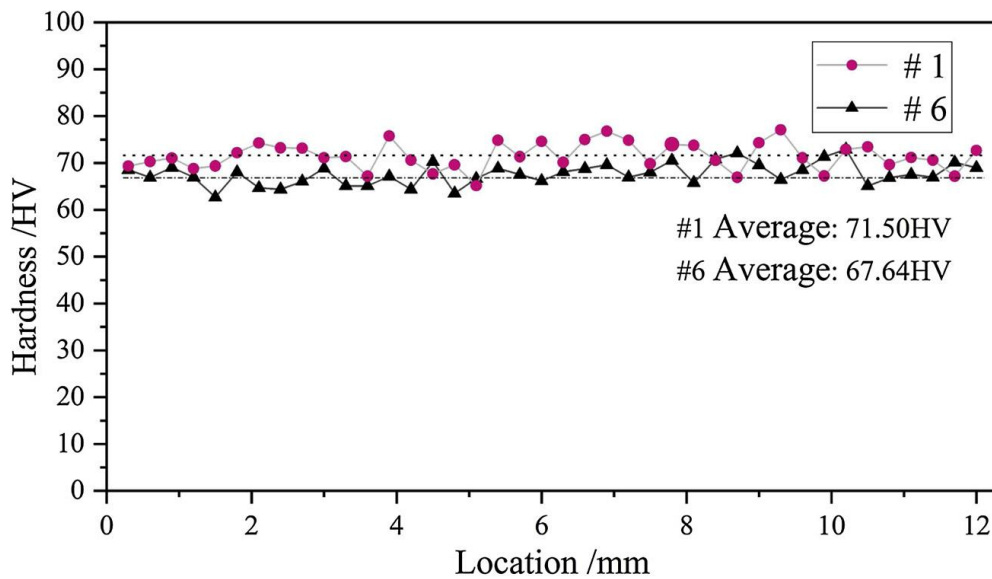


Figure 2.14: Hardness test results for sample [19]

In summary, the decrease in solute atoms caused by Magnesium loss led to diminished lattice distortion and a decreased capacity to obstruct dislocations. Consequently, this resulted in a decline in strength and hardness, accompanied by an increase in elongation. These findings offer significant insights into the intricate interplay between Magnesium content and the mechanical characteristics of Al-Mg alloys.

2.6 Beta Phase Formation

The β -phase Al_3Mg_2 formation is a critical aspect of this literature survey. This phase holds particular significance as it emerges at the grain boundaries of the component and also serves as an anode in the corrosion study of the sample. The β -phase's anodic characteristics along grain boundaries can promote the initiation of pitting corrosion on the surface of the component. Utyaganova et al. [10] Therefore, the identification and understanding of this phase are pivotal for advancing our knowledge in the field of corrosion studies.

In various research papers, the existence of the β -phase has remained documented through different techniques. In some cases, Wang et al. [17] XRD peaks clearly reveal the presence of the Al_3Mg_2 , while in SEM images, it is characterized by distinct black-colored regions on the surface. Additionally, certain studies Geng et al. [9] have indicated that the Al_3Mg_2 is precipitated when the composition consists of approximately 90% Al and nearly 5% Mg, a composition that is readily discernible through EDS analysis. Furthermore, in select instances, the β -phase is described as being in the form of nano-particles, detectable only through transmission electron microscopy (TEM). The diverse methods of identifying the Al_3Mg_2 highlight the complexity and variability of its characterization in the literature.

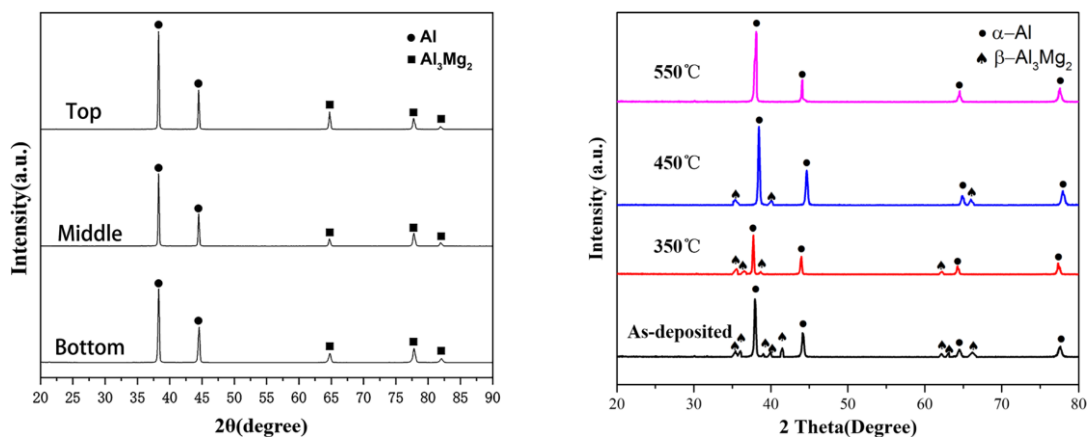


Figure 2.15: XRD graphs from different journals [5] [8]

2.6.1 X-ray Diffraction (XRD) and Elemental Analysis

To gain deeper insights into the microstructural differences observed in distinct regions, X-ray Diffraction (XRD) experiments were conducted on ER5356 alloy fabricated using WAAM in bottom region of wall. The XRD patterns in Fig. 2.16 reveals notable variations in peak intensities while maintaining consistent main features.

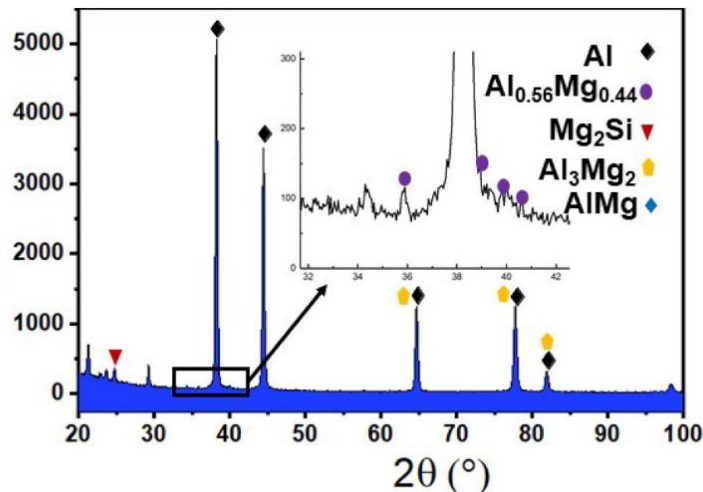


Figure 2.16: XRD graph [9]

2.6.2 Phase Identification

As reported by Geng et al. [9], the X-ray diffraction (XRD) pattern predominantly features strong intensity peaks corresponding to planes (111), (200), (220), (311), and (222), as illustrated in Fig. 2.16. These peaks are associated with the Aluminium phase and the precipitation of Al_3Mg_2 . Furthermore, weaker peaks suggest the presence of other phases, likely involving Aluminium and Magnesium (such as Al–Mg, $\text{Al}_{0.56}\text{Mg}_{0.44}$, and Al_2Mg). The formation of $\text{Al}_{0.56}\text{Mg}_{0.44}$ may be recognized to the low solubility of Magnesium in Aluminium, while the presence of low-content silicon in ER5356 may lead to the formation of Mg_2Si , detectable through XRD. Additionally, Al_5Mg_8 may be observed in the XRD pattern within the range of $2\theta = 35\text{--}43$ degrees. It's important to highlight that the lack of additional peaks indicates the absence of new crystalline phases, underscoring the uniformity of phase composition across different regions.

2.6.3 Elemental Analysis

To verify the composition of the β -phase, EDS analysis was conducted at various points within a randomly selected region. As illustrated in Figures 2.17 and summarized in Table 1, the grain boundaries, grain interiors, and the secondary phase

Predominantly comprise Aluminium (Al) and Magnesium (Mg), with the inclusion of some trace microelements.

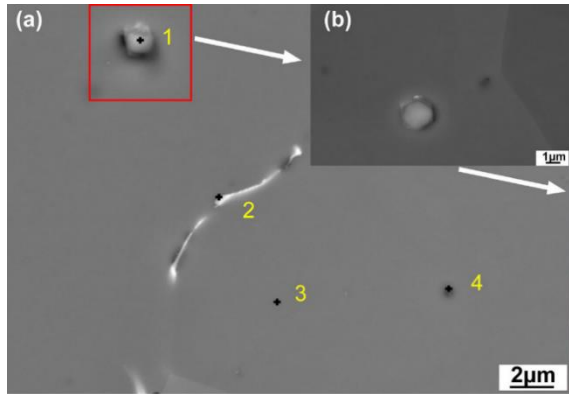


Table 2.3: Chemical composition of alloy

Number	Mg	Ti	Cr	Mn	Fe	Al
1	6.22	1.94	1.95	-	-	Bal.
2	3.95	-	-	1.04	8.81	Bal.
3	4.21	-	-	-	-	Bal.
4	4.71	-	-	-	-	Bal.

Figure 2.17: SEM image of sample [9]

A slight variance in elemental composition is evident among the four points in Fig. 2.17(a). Conversely, point 3 and point 4, situated within the grains, exclusively contain Magnesium (Mg) and Aluminium (Al). According to this analysis, different compounds are forming inside the second phase and along grain boundaries, and Magnesium is the second most common element in the microstructure. (Geng et al. [9])

The Magnesium distribution within grains and grain boundary is influenced by factors such as driving force, time and temperature. After the solidification of melt pool, Al-Mg precipitates tend to form preferentially near the ultrafine grain boundaries. Subsequently, Mg diffuses to regions with bottom Mg concentration as heat is transferred.

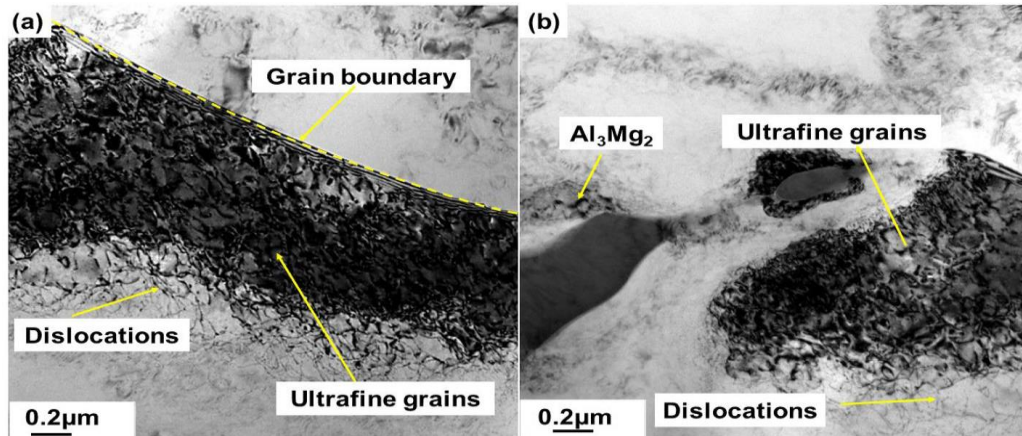


Figure 2.18: Transmission Electron Microscope (TEM) images of ER5356 samples produced by WAAM (a) in the direction parallel to the travel path, and (b) in the direction perpendicular to the travel path. [9]

2.7 High Pressure Torsion (HPT)

High-Pressure Torsion (HPT) is a sophisticated processing technique that plays a crucial role in investigating grain refinement and mechanical strengthening within materials, with a particular focus on Aluminium alloys.

This section explores the intricacies of HPT and its potential applications in advancing material science. In essence, HPT involves subjecting a material to extreme pressure and simultaneous torsional deformation. This process is executed at room temperature, utilizing pressures as high as 5 GPa. The core principle of HPT lies in its ability to induce severe plastic deformation, resulting in a profound impact on the microstructure. In this technique, the HPT process was applied to Aluminium alloy discs, and after just one revolution, a sub-micron grain structure was developed. The immediate improvement in hardness and tensile strength demonstrates how effective HPT is at enhancing the material's mechanical properties.

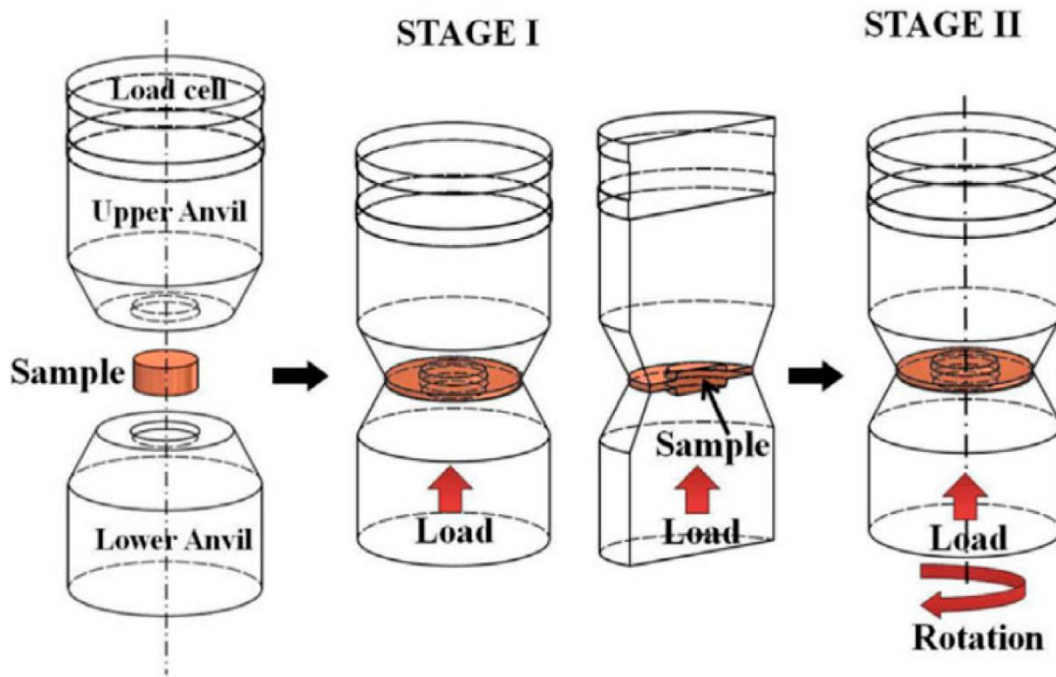


Figure 2.19: Diagram illustrating the HPT machine featuring the uniaxial compression stage (I) followed by the simultaneous torsion and compression stage (II) [46]

2.8 The Corrosion of Aluminium Alloys

2.8.1 Introduction

Since the earliest utilization of metals, corrosion has been acknowledged as a significant concern. Historical records from Roman times reveal that soldiers encountered rust on their weapons [1]. In the 1890s, as the availability of Aluminium metal increased sufficiently for industrial use, reports on Aluminium corrosion began to emerge.

Aluminium, being a thermodynamically reactive metal, is susceptible to oxidation. Figure 2.20 illustrates the potential E versus pH diagram (Pourbaix diagram) [42]. At a temperature of 25°C and within the pH range of 4 to 8.5, the oxide film formed on Aluminium serves as a protective barrier, offering excellent corrosion resistance. In the event of damage to the barrier oxide film, it has the capability to reform in most environments. Despite being only around 1 nm thick in ambient air conditions, this oxide film effectively shields the metal from further corrosion [43].

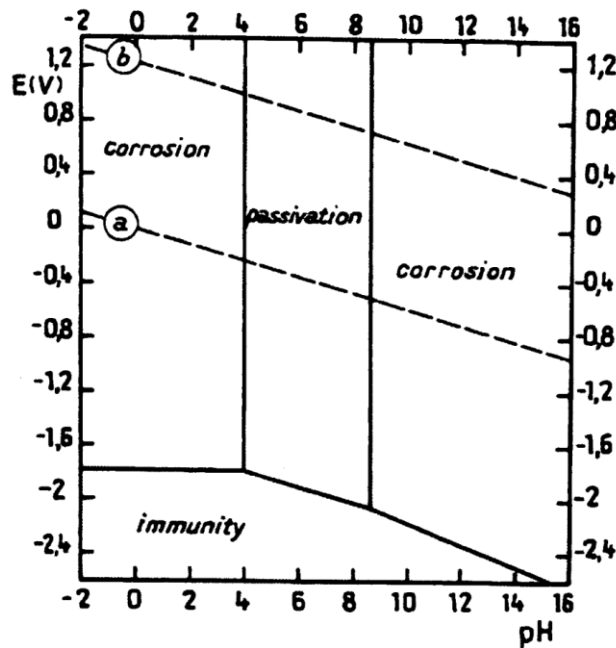


Figure 2.20: Theoretical realms encompassing corrosion, passivation, and immunity of Aluminium at a temperature of 25°C have been investigated, as depicted in the relevant study [42].

2.9 Effect of Alloying on Corrosion Behaviour

2.9.1 Pitting Corrosion

Pitting corrosion is a common occurrence across all Aluminium alloys. It manifests randomly and unevenly over the entire surface. The presence of crevices can locally accelerate pitting. Extremely pure Aluminium, with a purity of 99.99 wt. % or higher, exhibits higher pitting resistance, whereas any addition of alloying element tends to diminish this resistance. The 5xxx Al-Mg alloys demonstrate notable resistance to pitting corrosion. 5xxx alloys that have undergone cold-working and contain excess Magnesium beyond the solid solubility limit i.e. Over 3% may be susceptible to exfoliation and stress corrosion cracking when heated for an extended period of time at temperatures between around 80 and 175°C [46].

The incorporation of Magnesium enhances the strength of alloys, as observed in series such as the 5xxx. Addition of Mg alter the electrochemical potential of the Al alloy, thereby even when they are in solid solution they affects the corrosion resistance. Notably, Mg significantly shifts the potential in the anodic direction. Previous research suggests that localized corrosion occurs where beta phase particles tends to create localized galvanic cell with alpha phase in the presence of electrolytic medium [48-50].

2.9.2 Intergranular Corrosion

Intergranular corrosion (IGC) is characterized by its selective attack on grain boundaries rather than the grains themselves. This corrosion phenomenon occurs irregularly across the entire surface, mainly concentrated in the abrupt grain boundary region, and frequently goes ignored visually. The localization of IGC is attributed to variations in composition among intermetallics on the grain boundaries, higher solute grain interior and the solute-depleted grain margins. Despite its inconspicuous appearance, IGC progresses more rapidly than pitting corrosion. It typically reaches a self-limiting depth due to restricted oxygen and corrodent transport along the narrow corrosion path. However, once the limiting depth is attained, the intergranular attack spreads laterally. It's important to note that if IGC leads to splitting or exfoliation, it becomes non-self-limiting. Compared to pitting corrosion, IGC features sharper tips, which exacerbate stress and contribute significantly to corrosion fatigue [51, 52].

Aluminium-Magnesium alloys (5xxx), containing Magnesium concentrations below 3%, typically demonstrate significant resistance against intergranular corrosion (IGC). However, alloys with higher Magnesium content may become vulnerable to IGC if not appropriately manufactured and used at normal temperatures. Prolonged exposure to temperatures exceeding 27°C can trigger susceptibility, a condition often referred to as sensitization. The susceptibility of corrosion increases with content of Magnesium, time of exposure at higher temperature, and the extent of cold working [55].

In order to quantitatively evaluate the intergranular susceptibility of Aluminium-Magnesium (Al-Mg) alloys of 5xxx series, a nitric acid mass loss test method known as ASTM G-67 has been developed. This method assesses the susceptibility to IGC subsequent to exposure to elevated temperatures.

2.9.3 Stress Corrosion Cracking

Stress corrosion cracking (SCC) results from the combined effects of sensitization corrosion, tensile loading, and exposure to a corrosive environment like sea water. It manifests as a delayed failure process, with crack propagation typically occurring at a low rate ranging from 10^{-9} to 10^{-6} m/s [56]. Extensive testing is conducted to guarantee sufficient resistance, considering the potentially catastrophic consequences of failure due to this corrosion mode and the uncertainty surrounding the time to initiate failure [20].

2.8 Corrosion study of ER5356 alloy

This section delves into the corrosion characteristics of ER5356 alloy, shedding light on the types of corrosion that predominantly affect this material. It is imperative to recognize that corrosion poses significant challenges to the durability and performance of alloys, and comprehending the corrosion phenomena surrounding ER5356 is indispensable for optimizing its application in diverse industries. This section aims to provide an insightful overview of the corrosion mechanisms, including intergranular corrosion, stress corrosion cracking and pitting corrosion that predominantly influence ER5356 alloy.

It's important to remember that at temperatures lower than 200°C, Magnesium supersaturates Al-Mg alloys with concentrations of Magnesium surpassing 3.5 weight percent [66]. Although this supersaturation helps achieve solution strengthening, if the alloy works at sufficiently high temperatures during service, it may also cause the β -phase (Al_3Mg_2) to precipitate. Since the β -phase does not function as a hardening precipitate, its precipitation has no effect on the alloys' mechanical properties, but it greatly increases their vulnerability to stress corrosion cracking (SCC) and intergranular corrosion (IGC). After extended exposure, this phenomenon known as sensitization can happen even at very moderate temperatures, like 50°C.

Despite the inherent anticorrosion properties of Aluminium-Magnesium alloys due to the formation of protective oxide film, they can still display susceptibility to pitting corrosion in chloride rich environment.

Potentiostatic tests employing an Electrochemical Instruments potentiostat were used to assess corrosion resistance. This procedure involved submerging the sample under open-circuit conditions in a 3% NaCl solution until a stable potential value was reached. The reference electrode was a silver chloride electrode submerged in a 3M KCl solution, and the counter electrode was a graphite rod. The voltage was changed at a rate of 1 mV/s on the primary electrode plate, which had a working surface of 10 mm². To investigate the corrosion behavior of thin wall made up of Aluminium-Magnesium alloys by utilizing EBAM. The samples were taken from the top, middle, and bottom region of the wall.

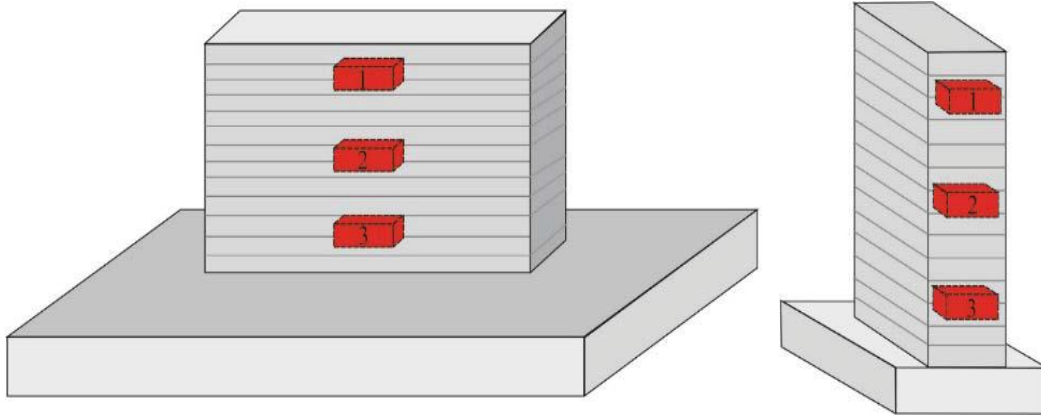


Figure 2.21: Schematic of Wall and Substrate [66]

Findings highlighted a clear connection between Magnesium content and corrosion resistance. As Magnesium content increased in the Aluminium solid solution, corrosion resistance decreased. This was evidenced by bottom corrosion potential and reduced corrosion current. Specifically, as Magnesium content ranged from 3.8% to 4.6%, we observed a decrease in corrosion potential from -0.806 to -0.984 V, and a decline in corrosion current from 2.13×10^{-9} to 1.92×10^{-10} A. Utyaganova et al. [66]

Table 2.4: Parameters of corrosion according to potentiostat tests

Number of sample	E_{corr} , V	I_{corr} , A	E_{pit} , V	I_{pit} , A
1 (upper)	-0.806	2.13×10^{-9}	-0.635	1.41×10^{-9}
2 (middle)	-0.928	1.79×10^{-9}	-0.627	1.82×10^{-9}
3 (lower)	-0.984	1.92×10^{-10}	-0.620	1.92×10^{-9}

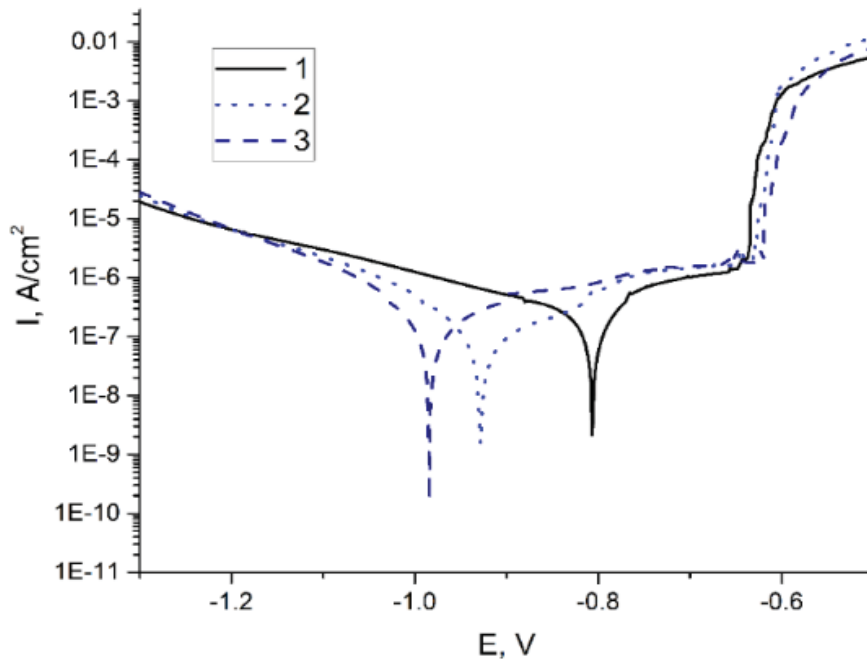


Figure 2.22: potentiostat dynamic plot [66]

Chapter 3

FINDINGS AND INSIGHTS FROM THE LITERATURE

- Acquired a dataset crucial for optimizing our WAAM setup for our machine.
- Obtained chemical compositions and results for various types of etchants suitable for 5xxx series Aluminium alloys, including:
 - Keller's Reagent[12]
 - Pulton's Reagent[15]
 - Weck's Reagent[16]
 - Modified Keller's Reagent[69]
 - Electrochemical Etching Using HBF₄[70]
- Unveiled notable variations in the microstructure across different regions of the wall. At the bottom region, the predominant microstructure consists of equiaxed grains with smaller grain size. As moving towards the middle region of the wall, the size of equiaxed grains gets larger and some columnar grains are also visible, As compared with the bottom region. However, the most significant contrast is observed in the top region, where grains are considerably larger. In this topmost section, equiaxed grains undergo a transition into columnar grains with clear directionality.
- Hardness testing results, revealing that the microhardness of the samples falls within the range of 65 to 80 HV without any heat treatment. With heat treatment, the hardness increases further to approximately 90 HV. Notably, the hardness of the interlayer is generally bottom than that of the inner layer due to the presence of pores and cracks.
- Tensile testing of as-deposited samples yielded valuable data. The yield strength ranges from 90 to 120 MPa, while the ultimate strength ranges from 190 to 280 MPa, with elongation reaching up to 40% at maximum. It's worth noting that the tensile stress in horizontal direction is higher than that of vertical direction in the wall due to interlayer defects.
- Revealed the impact of Magnesium evaporation during deposition. Mg loss is more pronounced at the top and minimal at the bottom of the wall due to temperature gradients. This leads to increased ductility at the top of the specimen, while hardness and tensile strength decrease as Mg loss from the sample increases.
- Identified the mechanism of beta phase Al₃Mg₂ precipitation along the ultrafine grain boundaries of the wall. Although this beta phase does not contribute to the alloy's hardness, it is susceptible to corrosion, leading to pitting corrosion on the alloy's surface.

- The HPT study revealed that subjecting the Aluminium alloy to extreme pressure and torsional deformation rapidly improved its mechanical properties. This led to the formation of a sub-micron grain structure, enhancing both hardness and tensile strength. While maintaining a relatively uniform composition with refined grains, the process's dynamic nature became apparent with some grain growth in subsequent revolutions.
- Gained insights into the corrosion behavior of Al alloy. While ER5356 exhibits excellent corrosion resistance, the presence of beta precipitates can lead to corrosion. Additionally data is collected on how to check corrosion resistance using mass loss tests and potentiodynamic polarization tests.

Chapter 4

OBJECTIVES

The primary objective of this research study is to investigate the feasibility and performance of Wire Arc Additive Manufacturing (WAAM) as a production method for ER5356 alloy components, with a specific focus on understanding the alloy's corrosion resistance and mechanical properties. The study aims to achieve the following specific research objectives:

1. **Assessment of WAAM Suitability:** Evaluate the applicability of WAAM as a viable manufacturing process for ER5356 alloy components, considering factors such as process parameters, material composition, and microstructural characteristics.
2. **Identification of Optimal Process Parameters:** Identify and recommend the optimal WAAM process parameters that result in improved corrosion resistance and desirable mechanical properties for ER5356 alloy.
3. **Mechanical Properties Characterization:** Examine the mechanical properties of ER5356 alloy produced through WAAM, including hardness and tensile strength. Determine the relationship between material composition, microstructure, and mechanical performance.
4. **Enhancing Mechanical Properties:** By doing appropriate heat treatments we are trying to improve the mechanical properties of the material by decreasing porosity and change in grain size.
5. **Corrosion Behaviour Analysis:** Investigate the corrosion resistance of WAAM-fabricated ER5356 alloy samples with varying Magnesium content. Analyze the corrosion kinetics, potential, and susceptibility to pitting corrosion in chloride-rich environments.
6. **Practical Applications and Industry Relevance:** Explore the potential applications of WAAM-processed ER5356 alloy in industries such as shipbuilding, mechanical engineering, aviation, and space technology. Assess its viability for load-bearing structures subjected to real-world conditions.

Chapter 5

EXPERIMENTAL WORK

5.1 Microstructure Characterization:



Figure 5.1: Wall manufactured by WAAM

5.2 Metallographic Sample Preparation

1. **Cutting:** Small pieces of the ER5356 alloy is cut with a wire-cut Electric Discharge Machine (EDM).



Figure 5.2: Cut Sample & FOSTEX FDK 7735 wires cutting EDM machine

2. **Mounting:** The specimens were hot mounted in Bakelite at approximately 200°C using a mounting press. The final mounted specimens had cylindrical shape with 15 mm height and 30 mm diameter. The edges of the mounts were rounded with a sand paper.

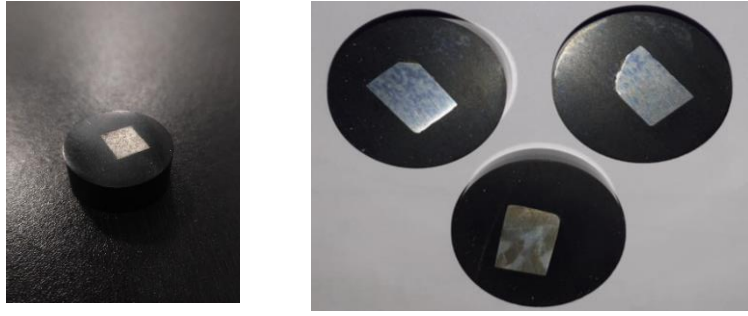


Figure 5.3: Mounted Samples

3. **Grinding:** The specimens were ground with grit papers of 180, 260, 400, 600, 800, 1000, 1200 and 1500 number in the stated order. Tap water was used as a coolant for grinding.



Figure 5.4: Grinding Operation



Figure 5.5: MetCo Bainpol Grinding/Polishing Machine

4. **Polishing:** Polishing was done with a soft cloth that is impregnated with diamond particles in a lubricant. We will be using diamond particles of size 3 microns and 1 micron in the stated order.



Figure 5.6: Polishing the Sample

5. Etching:

After polishing to observe the micro structure under a microscope, etching is performed using various etchants. This is because some etchants can reveal the grain structure clearly but may dissolve the beta phase, while others may damage the sample. We have tested six different etchants, and so far, the best results have been obtained with Weck's reagent. The composition of all the etchants, along with their respective results, is shown below.

1. **Poulton's reagent** : 50 ml of Poulton's reagent (2 ml HF, 3 ml HCl, 20 ml HNO₃, 175 ml water) + (50 ml HNO₃, 40 ml of solution of 3gm chromic acid per 10 ml water.), few drops on the surface for 1-4 minutes.
2. **Weck's tint etchant** : 100 ml water, 4 gm KMnO₄, & 1 gm NaOH, Best result shows in 30sec
3. **Keller's Etchant** : Distilled water 190ml, Nitric acid 5ml, Hydrochloric acid 3ml, Hydrofluoric acid 2ml, 10-30 second immersion
4. **Barker's reagent** : (5 ml HBF₄ 48% in 200 ml H₂O, 20 V)



Figure 5.7: Etchants for Etching

5.3 Characterization Techniques

A) **Optical Microscopy:** Optical microscopy is primarily done in order to understand the grain size and structure of the metal. To prepare a sample for optical microscopy, it needs to be cut, mounted, grinded, polished and etched so that the microstructure is clearly visible. Zeiss Axiovert A1 inverted microscope was used for take optical images of the sample.



Figure 5.8: Zeiss Axiovert A1 inverted microscope

B) **FE-SEM (Field emission scanning electron microscope):**

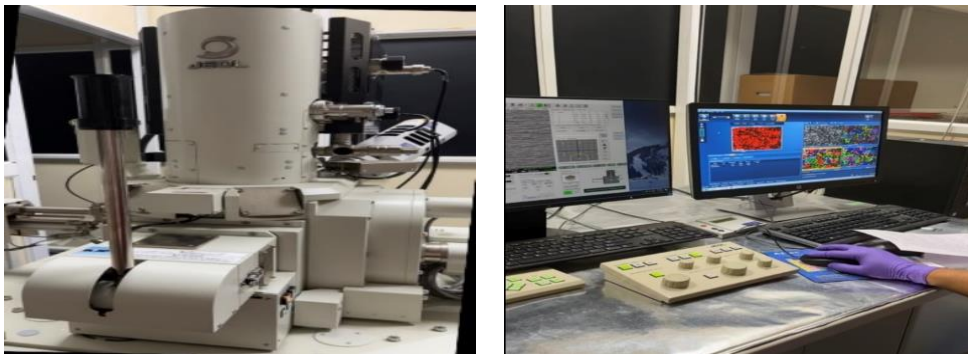


Figure 5.9: Field emission scanning electron microscope

It helped in looking at the intermetallic more clearly. JEOL-JSM-6500FPlus FE-SEM was used to look at the microstructure of the specimen by SEM and doing EDS on them.

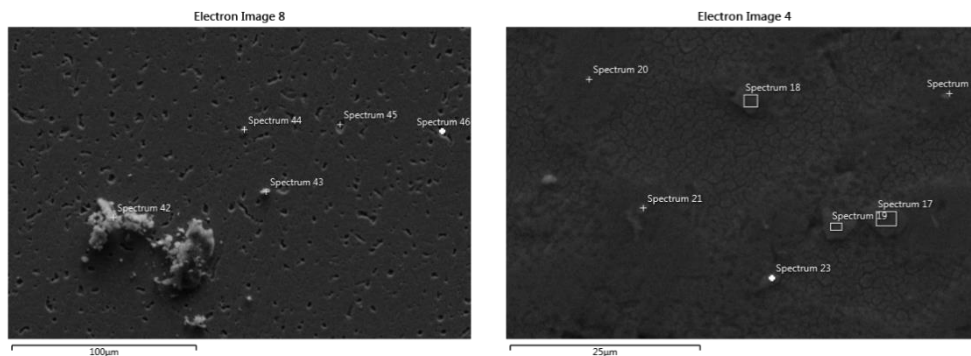


Figure 5.10: FE-SEM image of ER5356 sample

C) EDS: EDS stands for Energy Dispersive X-Ray Spectroscopy. It was used to figure out the elements present in the specimen and their composition (in wt. %). A compositional map was also created.

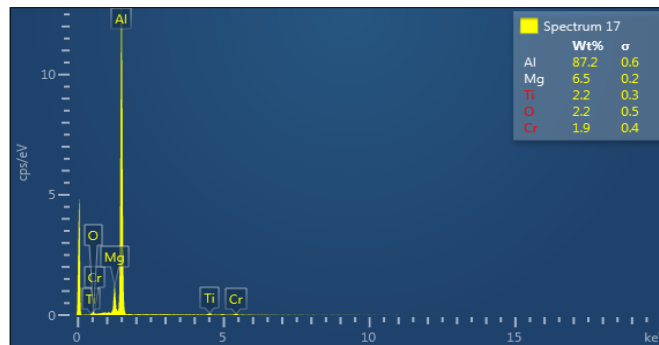


Figure 5.11: EDS image of ER5356 sample

D) XRD: X-Ray diffraction analysis (XRD) is a non-destructive technique that we used to find the peaks of beta phase and any other phases that may be present like Mg₂Si etc. XRD scanning is done on the top area of the wall in the range of 10° to 90° followed by scanning rates of 8degree/min and 1.6degree/min respectively.



Figure 5.12: PANalytical XRD machine

E) EBSD: The electron backscattered diffraction (EBSD) method was used to measure the average grain size and micro-texture analysis. The Aztec HKL program was used to analyse the data, which were collected using a FE-SEM with a 70 tilt sample at 15 amp current and 15 kV voltage. After the samples were mirror-polished, a last stage of cloth polishing with 0.04-micron-sized colloidal silica was performed for 60 minutes to get the samples ready for the EBSD scan.

5.4 MECHANICAL TESTING

- 1) **HARDNESS TEST:** The Vickers hardness test was performed to measure the hardness of materials, specifically the different sections from the wall including bottom, middle and top thin sections.



Figure 5.13: Hardness testing machine and samples

- 2) **TENSILE TEST:** Tensile testing was conducted to obtain data regarding the tensile strength, yield strength, and ductility of the material. Out of all the samples available for testing, we have tested twelve samples so far, namely H1, H2 and H3 for horizontal deposition and V1, V2 & V3 for vertical deposition. And same set of remaining six samples were tested after T6 heat treatment.



Figure 5.14: Tensile test specimens before testing

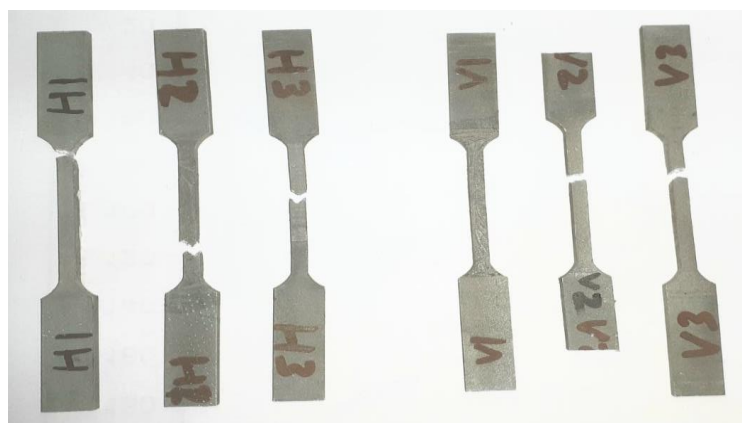


Figure 5.15: Tensile test specimens after testing

5.5 Corrosion testing

5.4.1 Nitric acid mass loss test (NAMLT)

NAMLT, conducted according to ASTM G67 standards. Rectangular sections of dimension 50 mm × 6 mm with thickness of 20 mm from each designated region (top, middle and bottom) of the wall were precisely prepared. This involved polishing starting from 180 grit and finishing with 1200 grit finish, followed by etching with a 5% NaOH solution and concentrated nitric acid to clean the surface of the sample. After thorough cleaning and drying, the initial weight and dimensions of each sample were documented. Subsequently, the samples were submerged in a nitric acid solution for 24 hours. After the test samples were cleaned, dried, and their final weight and dimensions were measured for analysis.



Figure 5.16: Immersed samples in nitric acid

5.4.2 Potentiodynamic polarization test (PDP)

Electrochemical testing is done by using a Metrohm Autolab PGSTAT101 workstation, a conventional three-electrode setup was employed using an Ag/AgCl reference electrode immersed in a 3M KCl solution, a graphite counter electrode, and the WAAM specimens as the working electrode. Rectangular specimens (10 mm × 20 mm) from all the three regions were extracted from the wall, cold-mounted to expose a 10 mm² surface area, and then underwent grinding and polishing for a uniform surface. The potentiodynamic polarization (PDP) curves were generated in a 3.5 wt% NaCl solution at a scan rate of 1 mV/s. Voltage measurements were recorded within a range of -1.2 V to -0.3 V relative to the reference

electrode. A total of nine samples were tested, three each from top, middle and bottom region of the as-deposited wall. To check the repeatability of the results, all tests were carried out for 3 times.

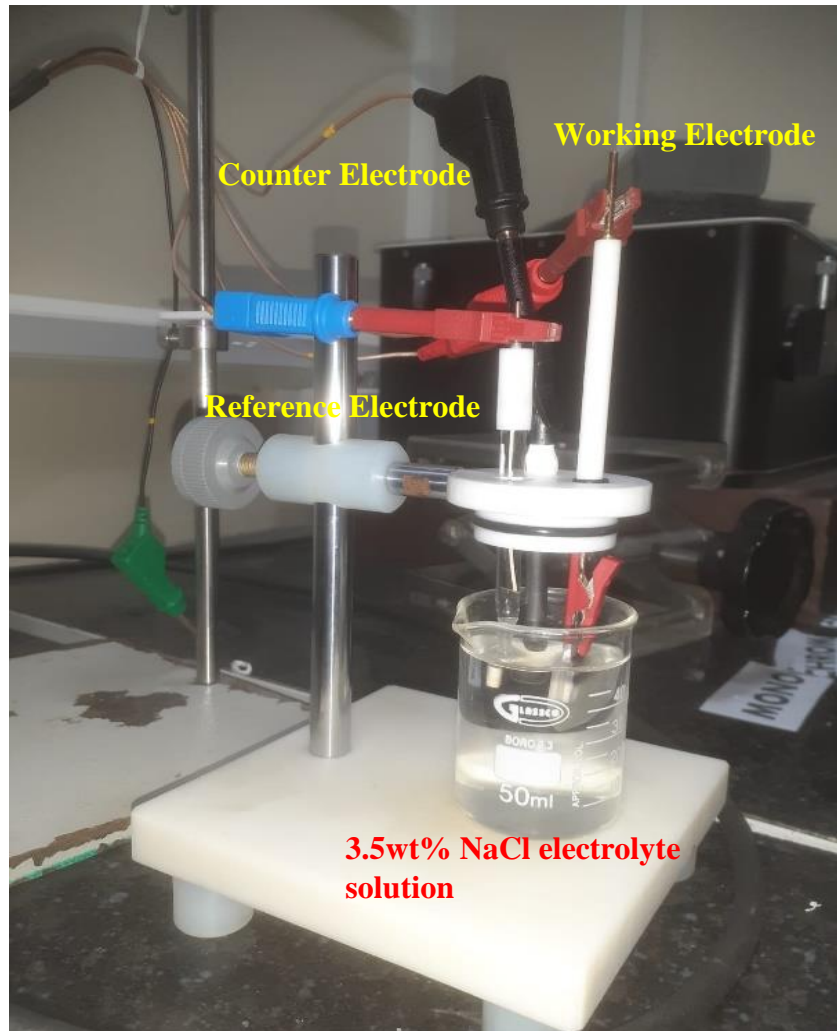


Figure 5.17: Potentiodynamic polarization corrosion test setup

Chapter 6

RESULTS AND DISCUSSIONS

6.1 Optical microscopy study of WAAM ER5356

By using Weck's reagent, the grains in the microstructure develop clearly, clear visibility of both the interlayer and inner layer, as shown in the figure 6.1 below.

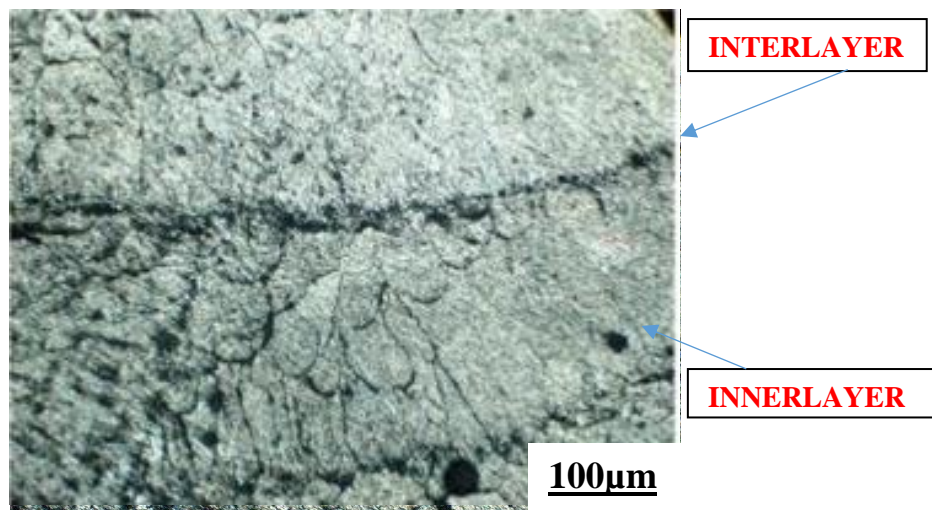


Figure 6.1: Optical microstructure of top area sample

As this sample is taken from the top side of the wall, columnar grains are clearly visible in the figure 6.2(a) and (b) below, also the intensity of pores is higher inside the interlayer.

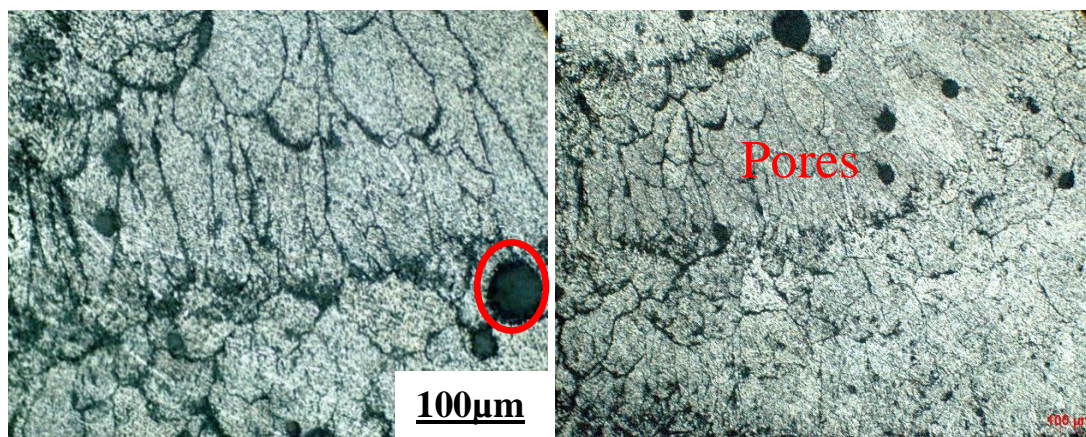


Figure 6.2: (a) columnar grains, (b) Inter layer

Figure 6.3 shows the optical microstructure after Keller's etched specimens but nothing is seen after the etching.

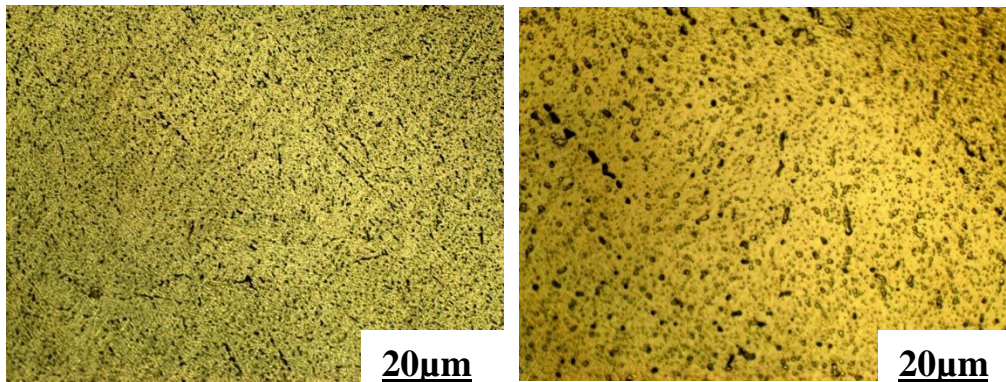


Figure 6.3: optical microstructure of Keller's etched specimen

6.2 SEM Study of WAAM ER5356

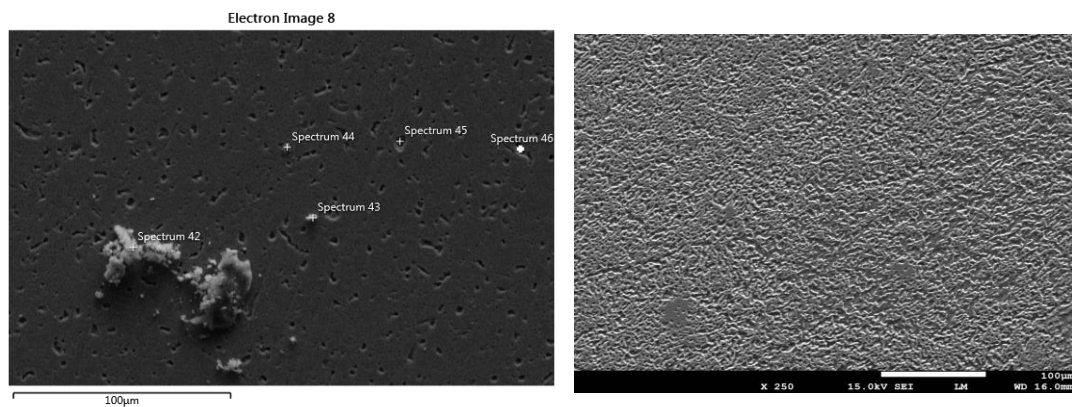


Figure 6.4: Pulton's Etchant (a)EDS & (b)SEM images

Fig 6.4 shows the images of SEM when sample is etched by PULTON'S reagent, here some phase is visible, after doing EDS of same sample it was found those are the oxide of oxygen and carbon, also the black spots are seen in this image are all Al and Mg only, EDS images are shown below in Figure 6.5 for reference:

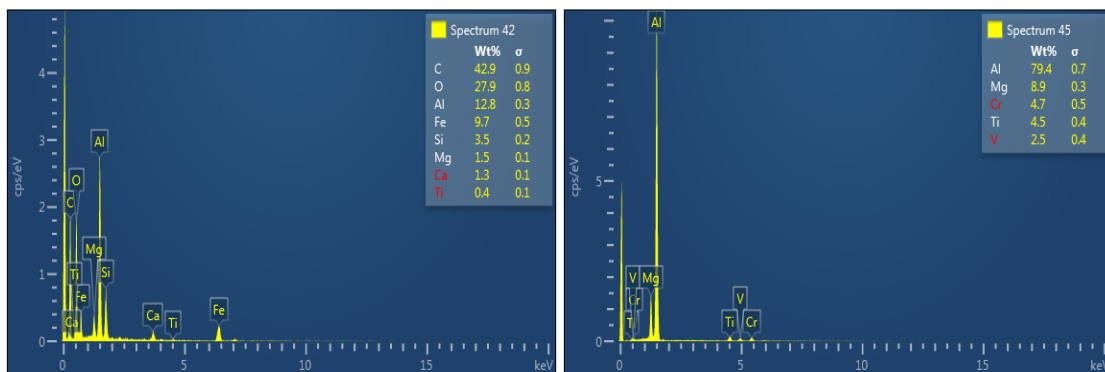


Figure 6.5: EDS Spectrum for Pulton's Etchant

Fig 6.6 shows the SEM images of the sample etched with Weck's reagent. In this image, grains are clearly visible, and some gray phases of Al and Mg are also visible. To confirm this, EDS mapping of these gray particles is conducted, and the EDS spectrum of the same particle is given below:

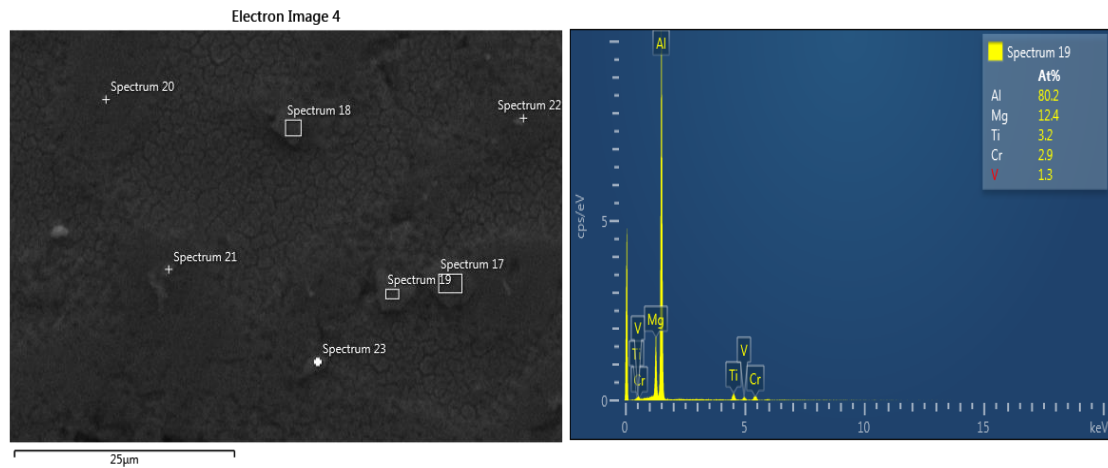


Figure 6.5 SEM and EDS for Weck's Etchant

- This mapping confirms that a phase of Al-Mg is formed by this process, likely Aluminium and Magnesium (such as Al-Mg, Al_{0.56}Mg_{0.44}, and Al₂Mg). As Al₃Mg₂ is nano sized particle and mainly distributed in the area close to grain boundaries it is not visible in SEM images [9].

6.3 EDS ANALYSIS

6.3.1 EDS Mapping Analysis

EDS mapping is conducted on non-etched samples in an attempt to locate the beta phase, but it has not been detected till now. While some particles are visible, subsequent scanning of these particles reveals the presence of Aluminium oxides with a composition of Al and O. Below are the images for reference:

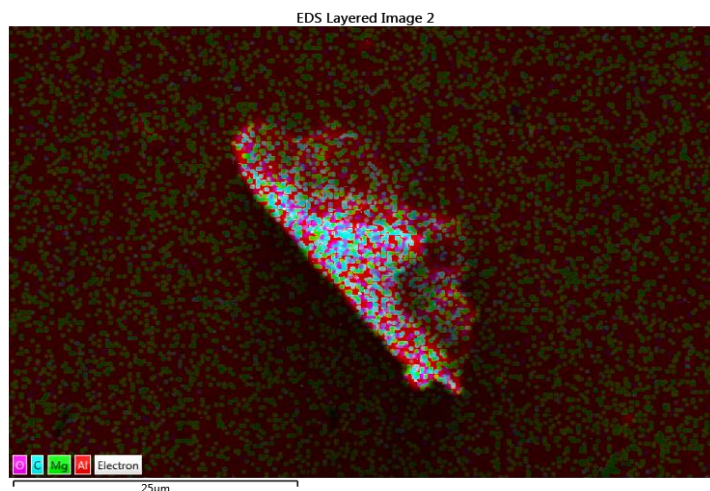


Figure 6.6: EDS layered image of non-etched sample

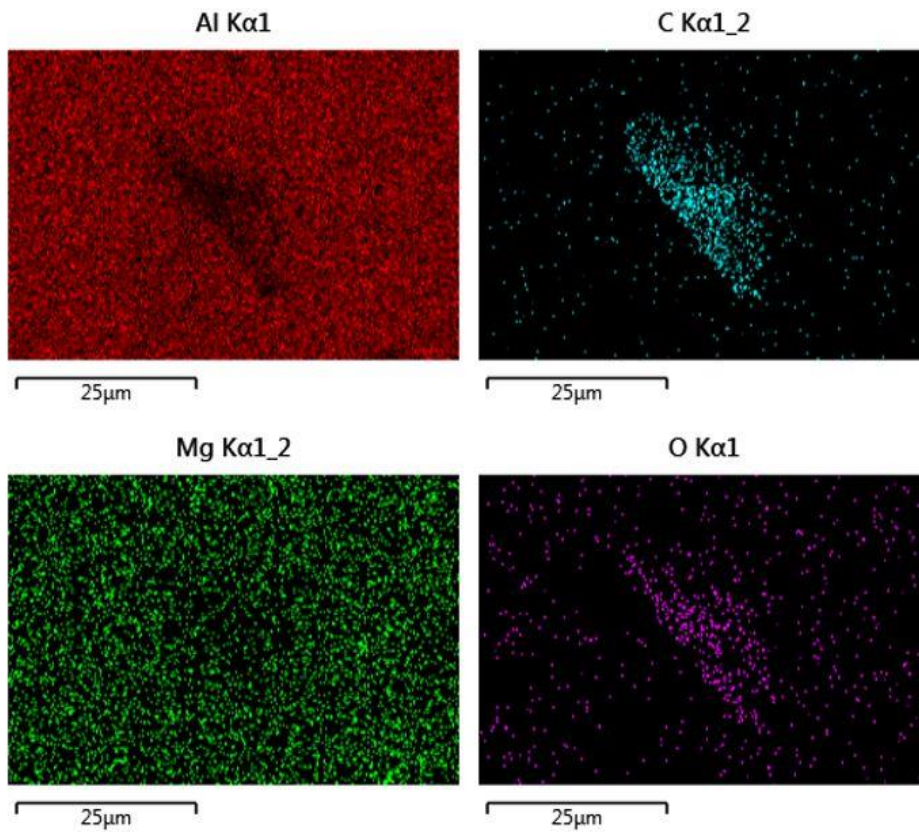


Fig 6.7: EDS mapping of non-etched sample

6.3.2 EDS point analysis

EDS point analysis of same non etched sample, spectrum 1 shows the chemical composition of that point.

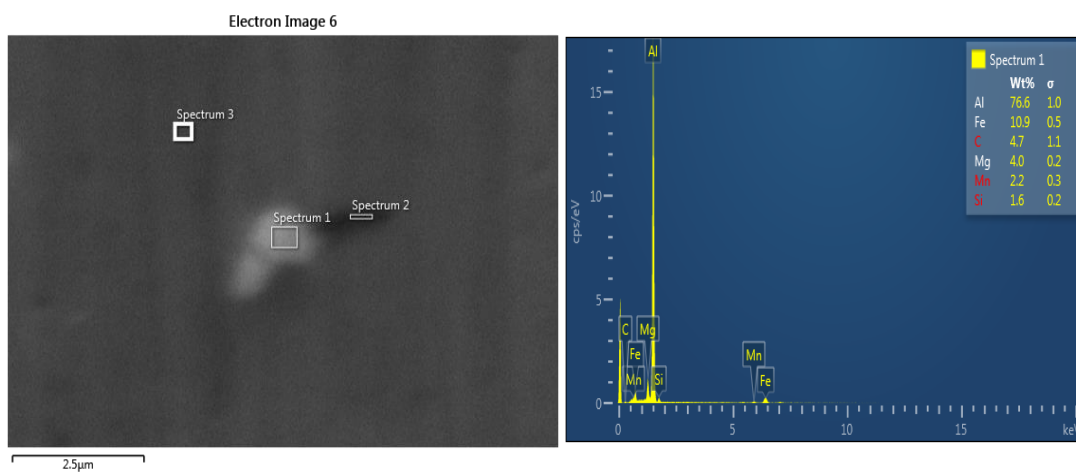


Figure 6.8: EDS point spectrum of non-etched sample

6.3.3 EBSD Analysis

Figure 6.9 depicts the EBSD maps of the top, middle, and bottom regions of the wall. As illustrated in Fig. 6.9, EBSD analysis reveals an increase in grain size along the building direction of the wall. In the bottom region, the average grain size (AGS) measures $33.3\ \mu\text{m}$, while in the middle it registers at $50.3\ \mu\text{m}$, and in the top region, it peaks at $55.4\ \mu\text{m}$. Additionally, the grains exhibit an almost equiaxed morphology throughout all regions because the EBSD is taken from the top plane of the sample (XY) to calculate the accurate grain size of the samples.

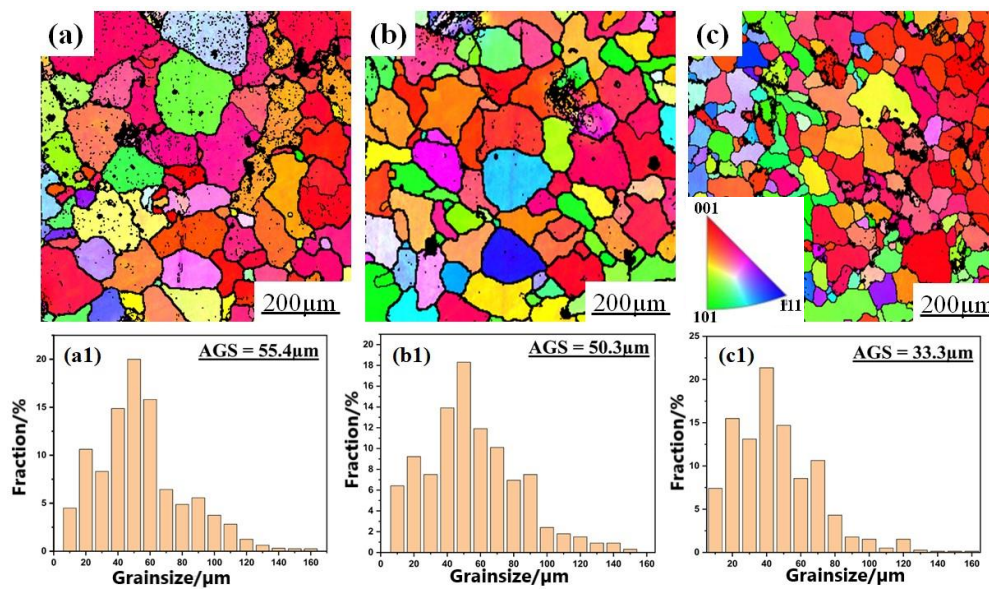
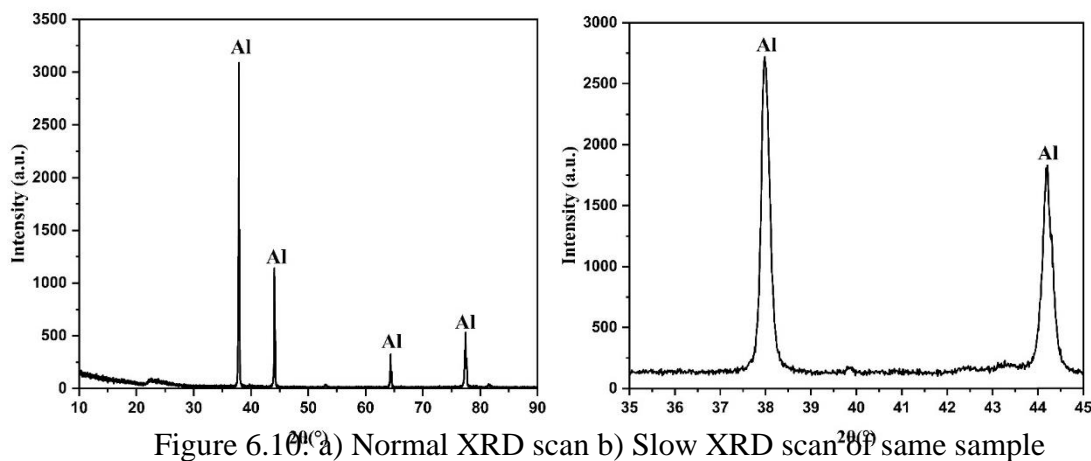


Figure 6.9: EBSD maps of a) top region b) middle region and c) bottom region of the wall along with their corresponding grain size distribution plot

6.4 XRD Analysis

Subsequent to XRD analysis, the same peaks are obtained corresponding to Al as reported in the literature. However, during EDS analysis of the same sample, identification the composition of Al_3Mg_2 is still not determined.

Furthermore, after conducting many XRD analyses on the same sample, one lasting approximately 8 minutes and the other around 50 minutes, still can't detect the beta phase. In the XRD results, a small peak is observed alongside the Al phase peak. After studying it confirms that those are the peaks of α_1 and α_2 and not the beta phase. Thus, based on XRD data, still it is not confirmed that the beta phase forms within the as-deposited sample or in the aged sample. XRD graph is provided below for reference: [44] [45]



6.5 Hardness Analysis

The hardness of the sample was measured using Vickers hardness testing.

- The hardness value observed was better than what was observed in the literature. All the readings follow a pattern of higher to bottom hardness values as we move from the bottom to the top due to the loss of Mg and heating effects during sample deposition.
- The topmost area has the least hardness value due to more porosity, while the bottom area has a higher hardness due to smaller grain size also in bottom near the substrate we got lesser hardness due to layer contains many micropores and cracks.

Table 6.1: Data for measured hardness values

TOP most	TOP	MIDDLE	BOTTOM	BOTTOM SUBSTRATE
69.61	70.01	74.56	83.3	76.01
66.92	73.4	76.01	86.2	77
66.51	70.7	77.5	85.63	77.5
67.93	71.36	79.28	82.5	76.26
66.71	73.16	78.01	80.87	78.77
75.04	71.81	79.29	81.41	73.87
69.05	71.58	79.56	78.52	75.35
70.25	71.8	77.01	84.19	75.77
69	71.72	77.65	82.827	76.566

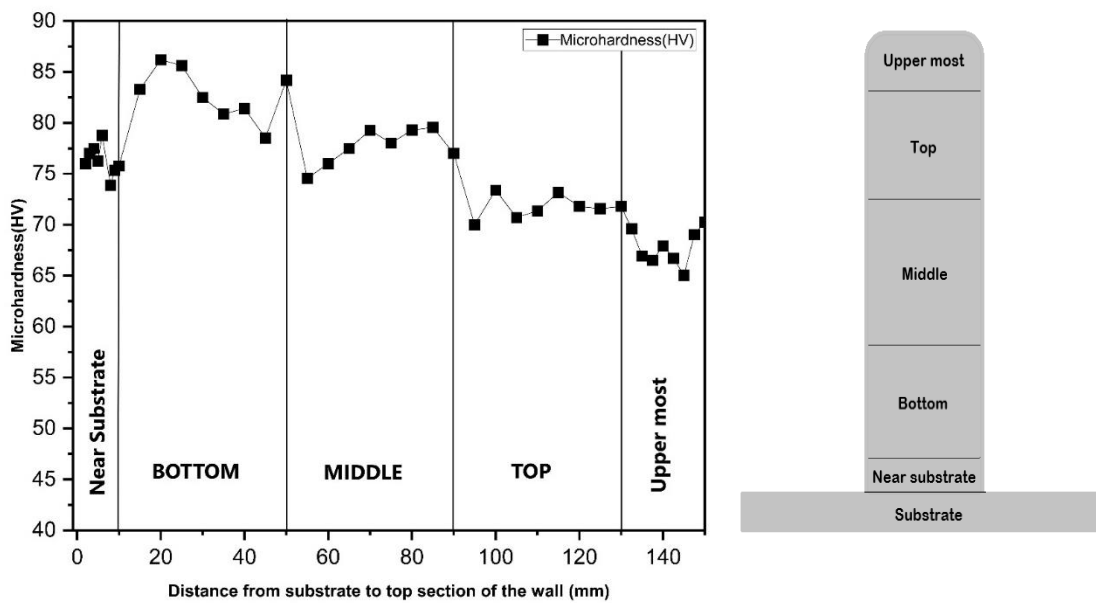


Figure 6.11: Hardness graph of different regions

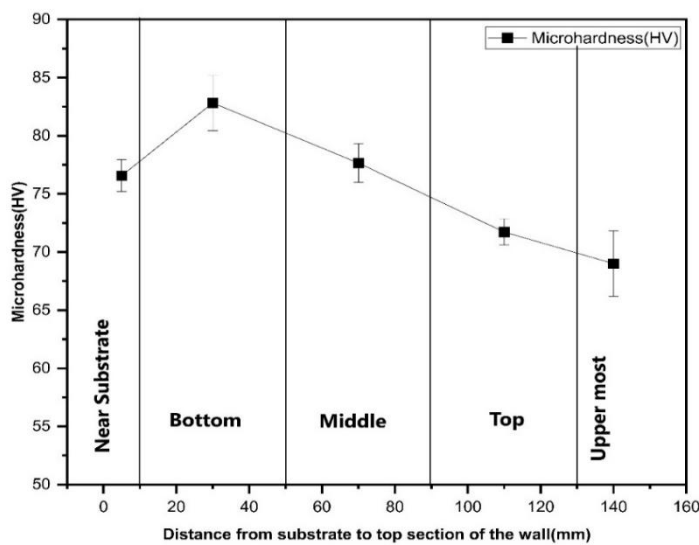


Figure 6.12: Hardness graph of different regions

6.6 Tensile Test Analysis

- Up to this point, tensile testing is conducted on twelve samples: three oriented horizontally and three oriented vertically in the building direction. Additionally, the remaining three samples are from horizontal and vertical regions, followed by solutionized heat treatment at 500°C for 12 hours.
- Test results show that horizontal tensile test specimens exhibit higher yield and ultimate tensile stress compared to vertical specimens. Specifically, for the as-deposited specimens, the yield strength (YS) was approximately 14% higher, and the ultimate tensile strength (UTS) was about 8.5% higher in the horizontal (deposition) direction compared to the vertical (building) direction.
- In the case of elongations, an opposite trend was observed. The elongation in the vertical direction was measured at 6.14%, whereas in the horizontal direction, it was observed to be 4.91%. This behavior may arise due to the presence of columnar grains in the building (vertical) direction.
- Following T4 heat treatment, there was a slight increase in yield strength (YS) and a noticeable enhancement in ultimate tensile strength (UTS) and elongation for both horizontal and vertical directions. In the horizontal direction, there was a 3% increase observed in YS, while in UTS, there was a 21% increase with an elongation increment of 61.8%.
- Similarly, for vertically oriented specimens, there was a 3.4% increase observed in YS, while in UTS, there was a 28.2% increase with an elongation increment of 66%.

The corresponding tensile stress-strain data table is provided below for reference:

Table 6.2: Stress strain data table from test results

		Yield Strength σ_y (MPa)	Ultimate tensile strength σ_{max} (MPa)	Elongation (%)
As-deposited	Horizontal	105.21 ± 2.8	162.82 ± 2.1	4.91 ± 1.4
	Vertical	89.53 ± 4.2	148.84 ± 2.7	6.14 ± 4.4
T4 Heat Treated	Horizontal	108.37 ± 3.1	206.37 ± 1.8	12.87 ± 1.9
	Vertical	92.72 ± 5.7	207.28 ± 3.0	17.96 ± 4.7

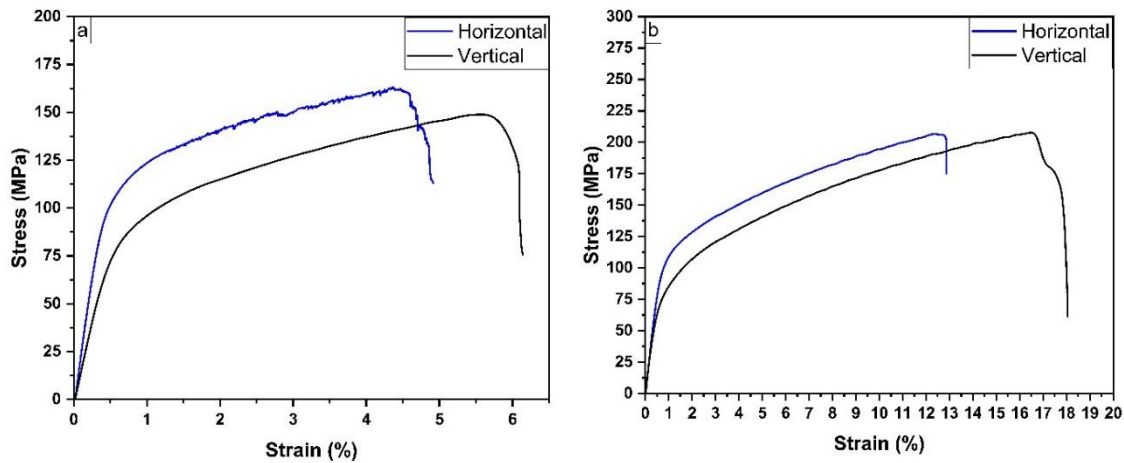


Figure 6.13: Stress strain curve a) for as deposited samples b) for solutionized samples

6.7 Heat Treatment

Two heat treatment processes were done on the samples. The first treatment involved solutionizing heat treatment in which samples were heated from 350°C, 500°C and 550°C starting from room temperature, holding at that temperature for 12 hours, followed by rapid quenching in water. The second treatment employed a similar initial stage of solutionizing heat treatment (Heating 500 °C for 12 hours) and subsequent quenching. However, it incorporated an additional aging step. After the quenching, the samples were reheated to 140 °C from room temperature and held at that temperature for a stabilization period of 7 days. Finally, the samples were taken out from the furnace and kept to cool till room temperature in the atmospheric condition. A schematic representation of both the heat treatment processes are provided in Fig. 6.14.

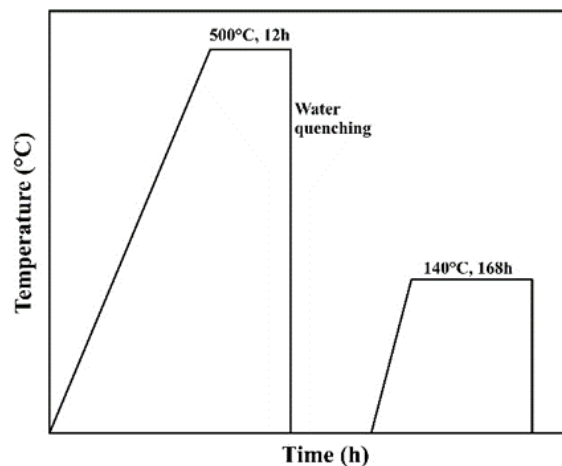


Figure 6.14: Solution heat treatment cycle

- At T4 at 350°C, a slight increment in hardness is visible. Subsequently, at 500°C, there is a more noticeable increment. However, after testing at 550°C, a decrement in

hardness is observed. Therefore, 500°C chose as the ideal temperature for T4 heat treatment and for further testing.

- After aging, the hardness and corrosion resistance of all samples decreased, even after 12 hours of aging. Therefore, it is decided not to perform aging for tensile testing.

6.8 High Pressure Torsion

High-Pressure Testing (HPT) is conducted on samples cut from the top portion of the wall, including those with half a turn, 1 turn, 2 turns, 5 turns, and 10 turns, respectively.



Figure 6.15: Dimensions of disk before and after HPT

Procedure of hardness measurement: To measure hardness, start moving from the center to the edge of the circular sample, with a difference of approximately 0.71mm in each reading.

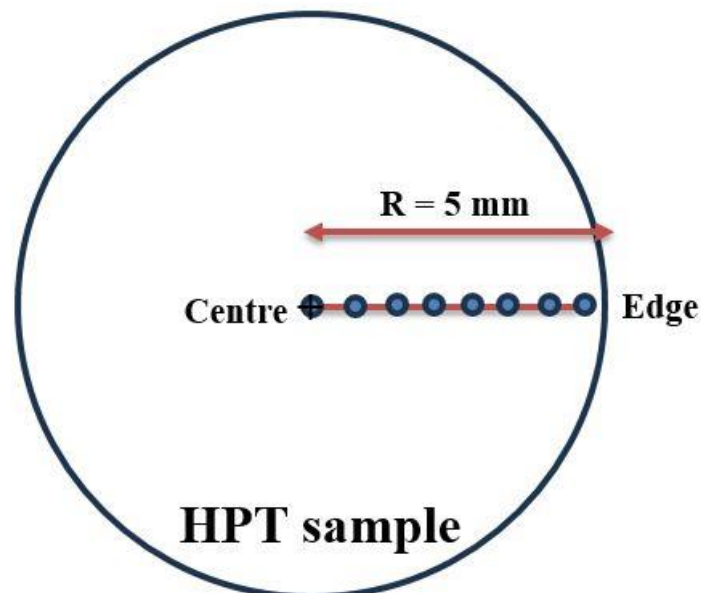


Figure 6.16: Microhardness measurement from centre to edge of HPT sample

- As seen from the below graph, hardness increases from 84HV (as deposited) to 205.4 HV (HPT). The hardness ranges from 141.42 HV for half a turn to 205.4 HV for five turns.

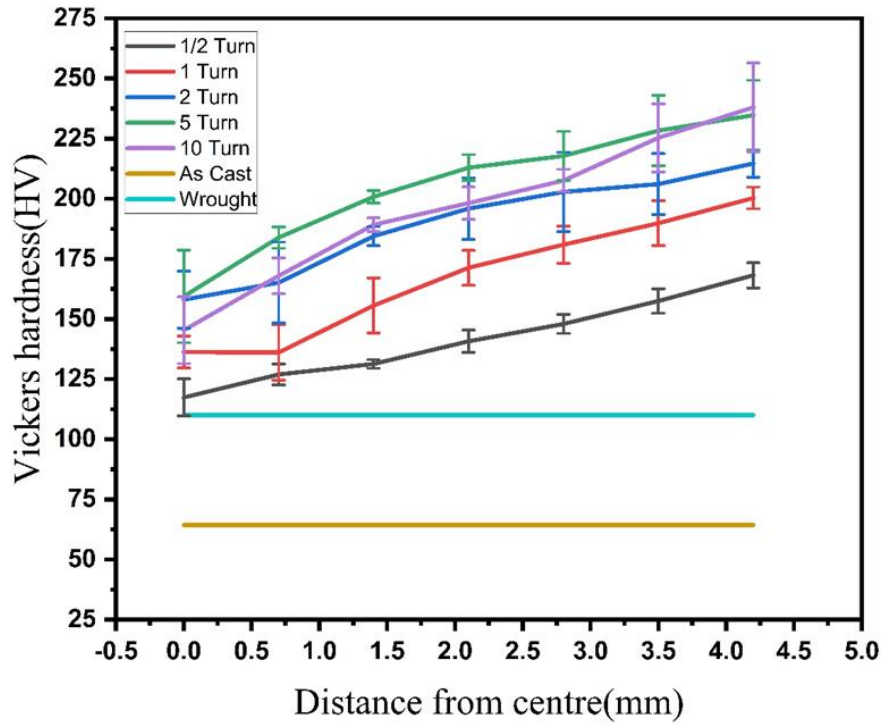


Figure 6.17: Microhardness of top area HPT sample

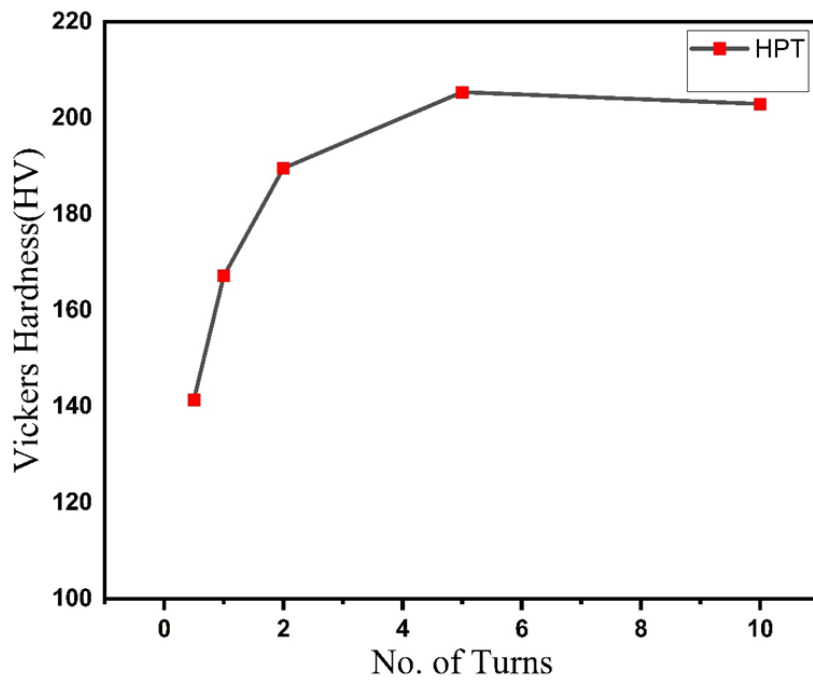


Figure 6.18: Microhardness comparison of top area HPT sample

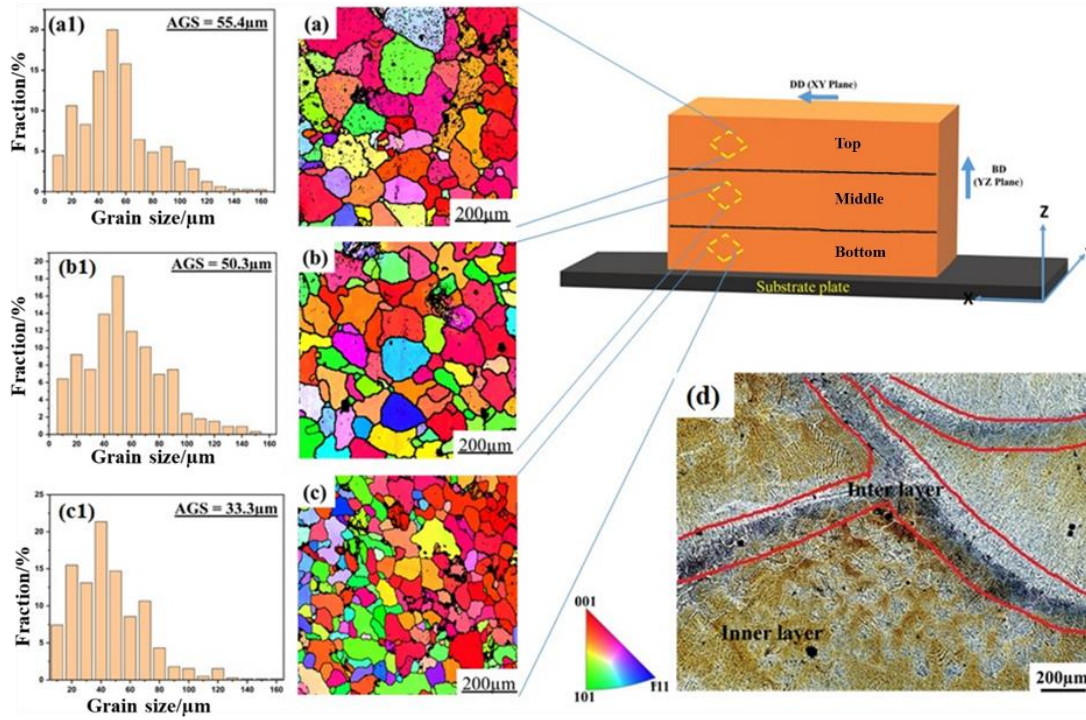
6.9 Corrosion test analysis

6.9.1 Microstructural effect on corrosion:

The homogeneity of chemical composition, grain size, and its distribution, as well as the content of intermetallic phases, plays a significant role in influencing the corrosion behavior of WAAM-deposited Aluminium alloys. Figure 6.19 depicts the EBSD maps of the top, middle, and bottom regions of the wall. As illustrated in Fig. 6.19, EBSD analysis reveals an increase in grain size along the building direction of the wall. In the bottom region, the average grain size (AGS) measures 33.3 μm , while in the middle it registers at 50.3 μm , and in the top region, it peaks at 55.4 μm . Additionally, the grains exhibit an almost equiaxed morphology throughout all regions because the EBSD is taken from the top plane of the sample (XY) to calculate the accurate grain size of the samples. This variation in grain size profoundly influences the corrosion characteristics of the component. Fig. 6.19 (d) shows the optical micrograph from the bottom region of the wall, where a clear difference in the inner layer (formed by single deposition) and interlayer (formed between two successive inner layers) is visible. The interlayer acts as a more preferential site for beta phase formation because of a higher grain boundary area compared to the inner layer.

The change in the average grain size can also be observed from Fig. 6.19 based on different regions of the wall. The average grain size has an obvious effect on corrosion resistance; smaller grain promote more preferential sites for beta phase precipitation from the alpha matrix. So, when the sample is kept in a corrosive environment like saltwater, galvanic cell formation occurs, in which the beta phase acts as an anode and the alpha acts as a cathode. Due to this, oxidation occurs on those preferential sites, creating pits on the surface of the sample. As shown in Fig. 6.19a in the top region of the wall, where grains are larger and the grain boundary area is bottom, there might be fewer preferential sites for the precipitation of the β -phase. Additionally, greater heat convection from the top region of the wall limits the formation of the β -phase, making this region less susceptible to corrosion. Conversely, in the bottom region (Fig. 6.19c), grains are smaller and the grain boundary area is higher, supporting sufficient preferential sites for β -phase precipitation. Also, the large heat transfer from the wall to the substrate via conduction as well as convection from atmospheric air results in the formation of smaller grains, with moderate susceptibility to corrosion. In the middle region (Fig. 6.19b), a combination of small and large grains coexists, with a moderate grain boundary area. While this region supports β -phase precipitation, there is also increased heat entrapment between the top and bottom regions of the wall because at that time, the wall was losing heat from the top

and bottom regions and not able to lose heat rapidly from the middle region. This promotes more heterogeneous precipitation of the β -phase inside the middle region from the alpha matrix, thus promoting more corrosion. In summary, corrosion susceptibility directly correlates with the grain size of the component: larger grains lead to reduced precipitation and consequently less corrosion.



Figure

6.19: EBSD maps of a) top region b) middle region and c) bottom region of the wall along with their corresponding grain size distribution plot, (a1) top region (b1) middle region and (c1) bottom region also (d) shows the microstructure of as-deposited sample

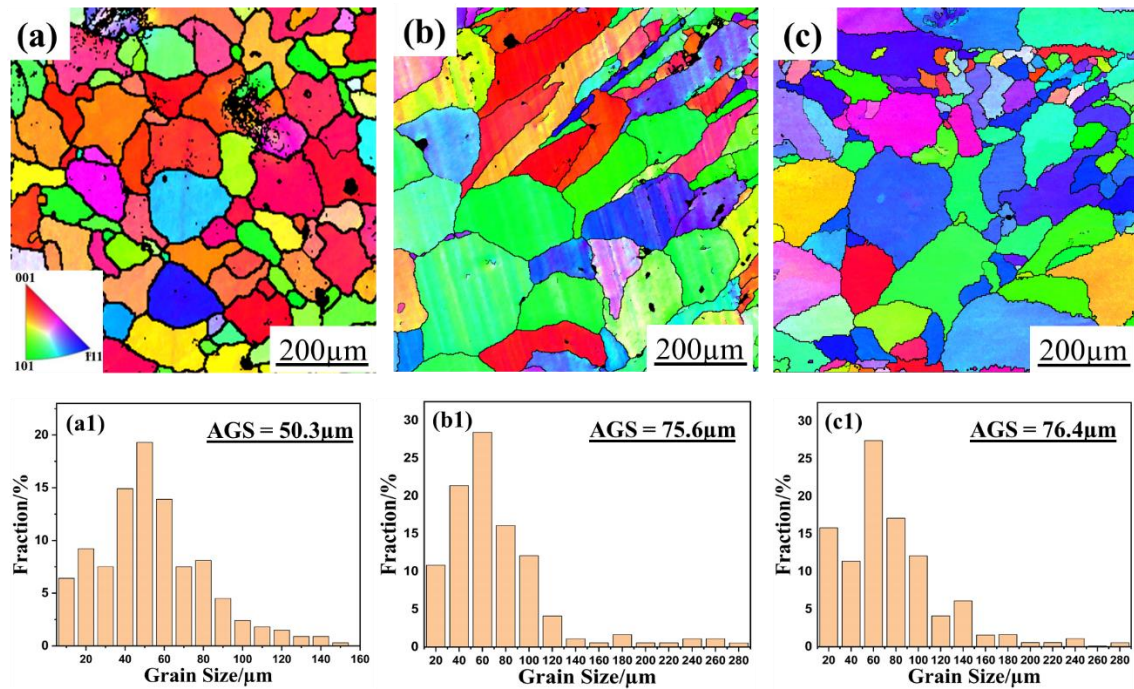


Figure 6.20: EBSD maps of middle region of the wall a) As-deposited b) after solutionizing c) after ageing heat treatments with their corresponding grain size distribution plot, (a1) as deposited (b1) solutionized (c1) aged

Figure 6.20 shows the EBSD maps of as-deposited, solutionized and aged samples. On the as-deposited sample, the average grain size (AGS) measures 50.3 µm, while in the solutionized it registers at 75.6 µm, and on the aged samples, it shows 76.4 µm. Additionally, here also the grains shows an almost equiaxed morphology throughout all samples as EBSD is taken from the top surface of the sample(XY plane). As discussed previously corrosion susceptibility directly correlates with the grain size of the component (larger grains lead to reduced precipitation and consequently less corrosion). As depicted in Fig. 6.20, EBSD analysis reveals an increase in grain size after the solutionized and ageing heat treatment this promotes less precipitation sites for beta phase and hence decreases the susceptibility of corrosion.

6.9.2 Nitric Acid Mass Loss Test

The Nitric Acid Mass Loss Test (NAMLT) was utilized to measure the degree of sensitization (DoS) of the WAAM-deposited AA5356 alloy. This test provides insights into the material's susceptibility to intergranular corrosion (IGC). As shown in Fig. 6.21, three samples were extracted from each designated region (top, middle, and bottom) of the additively manufactured as-deposited wall. The results, presented in Table 6.3 and Fig. 6.21, reveal variations in mass loss across the samples from the top to bottom region. The middle region shows a mass loss of

$7.73 \pm 0.35 \text{ mg/cm}^2$, which is the highest among the other two regions compared to the top ($3.89 \pm 0.29 \text{ mg/cm}^2$) and bottom ($4.79 \pm 0.23 \text{ mg/cm}^2$).

Aluminium possesses a property that it does not react with nitric acid due to the formation of an Al_2O_3 film on its surface after reacting with atmospheric oxygen. This Al_2O_3 film acts as a passive layer, making the Aluminium resistant to corrosion. However, if the beta phase is present on the surface of the Aluminium, it hinders the formation of the Al_2O_3 film, creating open sites for pitting and IGC on the metal surface. This test was conducted to check for the presence of the beta phase. If the beta phase is present on the surface, its dissolution occurs within the nitric acid, resulting in mass loss from the sample's surface. This mass loss is then calculated to assess the susceptibility of IGC.

Fig. 6.22 shows the digital images of middle region samples from the wall, images of only middle is shown because it shows the maximum weight loss per cm^2 of area as per our previous section of as-deposited samples. Fig 6.22(a) shows the polished surface of as-deposited sample just to compare before and after effects of the test. Fig 6.22 (b) shows the presence of cracks in the as-deposited sample after immersion, suggesting a potential correlation with the presence of β -phase at a surface. In contrast, the solutionized sample Fig.6.22 (c) exhibits no visible cracks after the immersion, indicating a potentially bottom β -phase content. Furthermore, the aged sample Fig.6.22 (d) displayed a significantly higher number of cracks and surface irregularities compared to the as-deposited and solutionized conditions. This observation aligns with the conception that the seven-day aging treatment promotes higher concentration of the β -phase also prolonged exposures at low temperatures (around $50 \text{ }^\circ\text{C}$) can induce Magnesium diffusion in AA5356 alloys with Mg content exceeding 3 wt% . This diffusion process leads to Magnesium enrichment at grain boundaries, exceeding the solid solution limit and promoting the heterogeneous nucleation and growth of the β -phase to reduce the stored energy within the material. It is well established that a higher β -phase content can negatively impact the corrosion resistance of AA5356 alloys. Therefore, the observed cracking and surface irregularities in the aged samples are likely because of the detrimental influence of the elevated β -phase concentration. Also the interlayer region is mostly affected by the nitric acid because grain boundary area is higher inside interlayer which supports more precipitation of beta phase. As shown in Table 6.3, all the values fall within the range of 0-15 mg/cm^2 , indicating that all regions are resistant to intergranular corrosion, or in other words, the concentration of the beta phase is not significant enough to affect the corrosion resistance of the alloy.

Table 6.3 – Test data for NAMLT test

Sample	Region	Mass loss(mg/cm ²)
AS- DEPOSITED	Top	3.89 ± 0.29
	Middle	7.73 ± 0.35
	Bottom	4.79 ± 0.23
SOLUTIONIZED	Top	3.24 ± 0.24
	Middle	5.09 ± 0.32
	Bottom	2.34 ± 0.28
AGED	Top	4.24 ± 0.22
	Middle	8.19 ± 0.29
	Bottom	6.58 ± 0.25

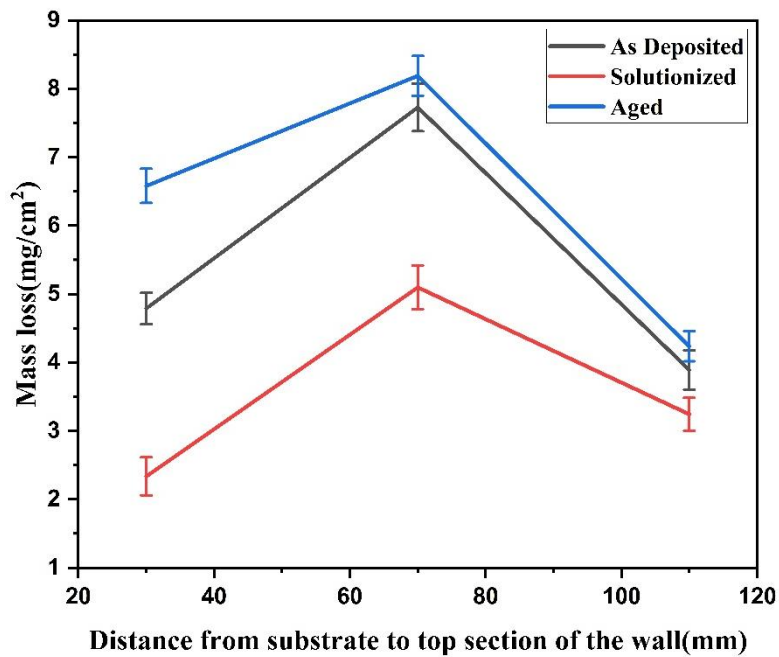


Figure 6.21: NAMLT test readings from different regions of the wall

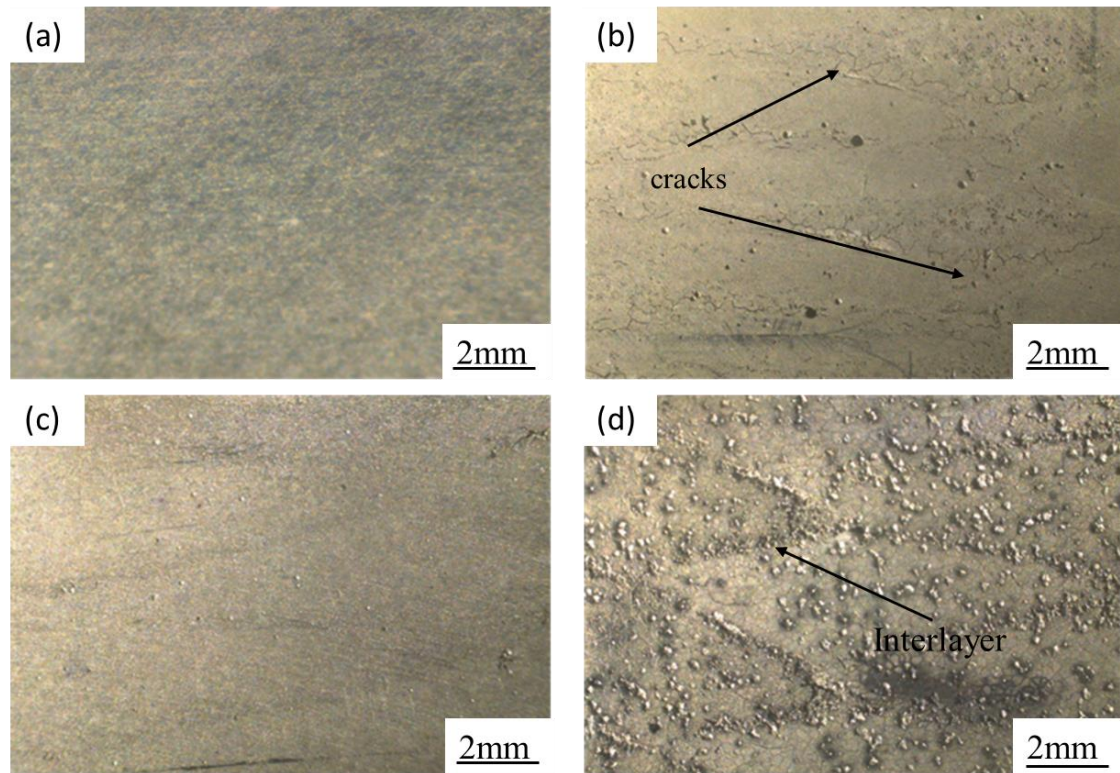


Figure 6.22: Represents the digital images of the middle region sample from a) as deposited b) as deposited after the immersion c) solutionized after the immersion d) aged after the immersion for 24hrs in nitric acid.

6.9.3 Potentiodynamic polarization test:

Potentiodynamic polarization test were conducted to assess the influence of corrosion behaviour on WAAM samples in similar region vice variation (top, middle & bottom) as previous, Fig.6.23 shows the obtained Tafel plots for the as-deposited samples of all three regions from the wall. Table 6.4 shows the relevant polarization test results of different regions from the wall. As shown the E_{corr} of top region shows least negative value -0.681 ± 0.003 V followed by -0.695 ± 0.002 V at bottom and -0.697 ± 0.004 V at middle region of the as-deposited wall. Also the corrosion current density become least $5.42 \pm 0.5 \times 10^{-6}$ A/cm² at the top region and highest $7.04 \pm 0.7 \times 10^{-6}$ A/cm² at the middle region of the wall. To calculate the rate of corrosion following equation is used,

$$\text{Corrosion rate (mmpy)} = 0.00327 * I_{\text{corr}} (\text{Eq. Wt}) / \text{Density}$$

$$[\text{Eq. Wt} = 9.113 \text{ g/mol}]$$

$$[\text{Density} = 2.641 \text{ g/cm}^3]$$

The results of the potentiodynamic polarization test confirmed the similar corrosion kinetics between the top, middle and bottom region of the wall. The WAAM-deposited AA5356 alloy in the as-deposited condition possibly to exhibited coarse and continuous intergranular intermetallic phases. These features hinder the formation of a uniform passive film on the metal surface. Consequently, the as-deposited samples possess poorer pitting resistance. These regions with coarse intermetallics and weak passive films become preferential sites for pit initiation, leading to increased pitting sensitivity.

Additionally, the chemical homogeneity of the alloy also plays a crucial role in corrosion resistance. Intergranular intermetallic phases (primarily Al₃Mg₂) exhibit a more negative corrosion potential compared to the α -Al matrix. This creates a scenario where the intermetallic phase acts as the anode, while the α -Al matrix functions as the cathode, forming localized galvanic cells at grain boundaries. The tendency for localized galvanic corrosion correlates directly with the potential difference and the respective areas of the anode and cathode phases. The observed trends in corrosion potential and current density directly correlate with the explanations provided above that the middle region has the maximum rate of corrosion followed by bottom and least at the top region of the wall.

Table 6.4 - corrosion rate of different samples

Sample	Region	Corrosion potential(v)	Corrosion current density (A/cm ²) x 10 ⁻⁶	Corrosion rate (mm/yr)
AS- DEPOSITED	Top	-0.681 ± 3	5.42 ± 0.5	0.0611 ± 0.002
	Middle	-0.697 ± 4	7.04 ± 0.7	0.0794 ± 0.007
	Bottom	-0.695 ± 2	6.38 ± 0.3	0.0719 ± 0.002
SOLUTIONIZED	Top	-0.645 ± 2	3.11 ± 0.2	0.0351 ± 0.004
	Middle	-0.679 ± 5	5.69 ± 0.5	0.0642 ± 0.006
	Bottom	-0.655 ± 4	4.48 ± 0.4	0.0505 ± 0.004
AGED	Top	-0.661 ± 3	3.77 ± 0.7	0.0426 ± 0.003
	Middle	-0.703 ± 6	8.59 ± 0.9	0.0971 ± 0.005
	Bottom	-0.726 ± 2	6.77 ± 0.4	0.0763 ± 0.007

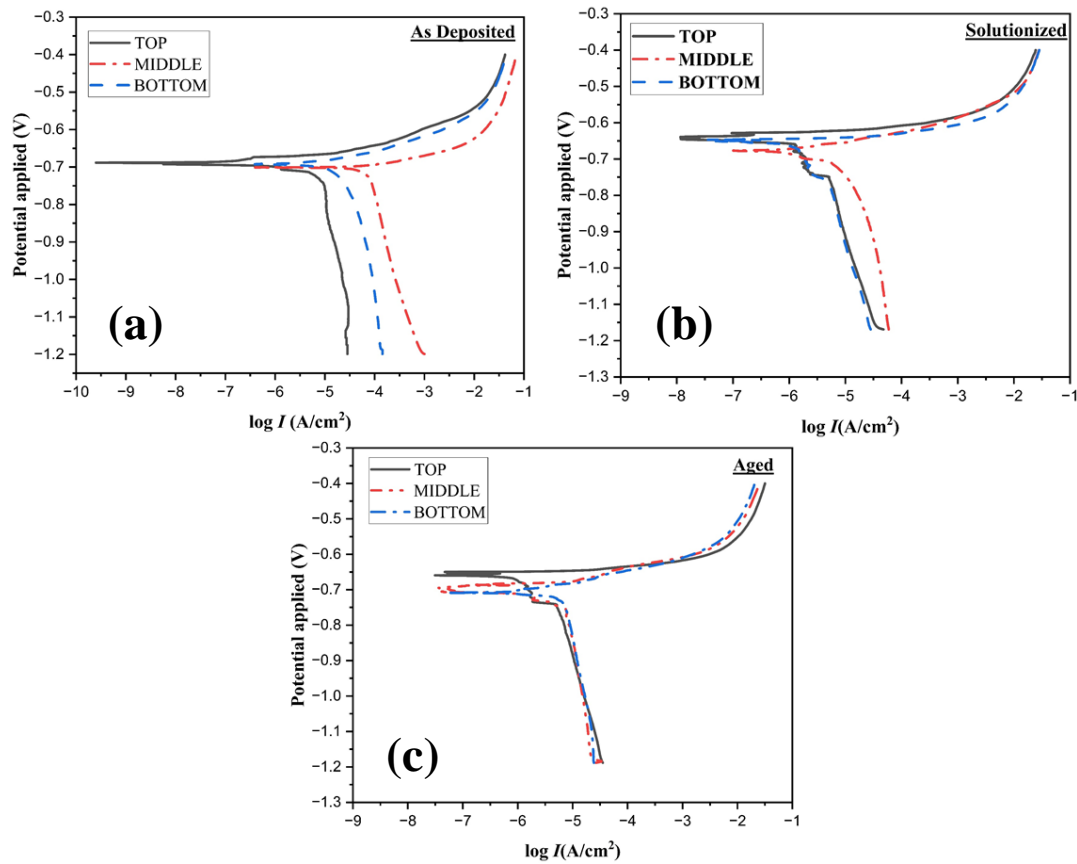


Figure 6.23: Tafel plots of a) As- deposited b) solutionized and c) Aged samples

Potentiodynamic polarization tests were again repeated after the heat treatment (solutionizing and aging) of WAAM samples. Fig. 6.23 shows the obtained Tafel plots from all the three regions of the wall for as-deposited, solutionized, and aged samples but images are shown only from middle region because it is that region which is mostly affected by corrosion. The relevant polarization test results are presented in Table 6.4. Analysis of the curves shows similar corrosion kinetics across the different treatment conditions.

Table 6.4 shows the corrosion rate of different regions from the wall before and after the heat treatments. As shown, the E_{corr} of the solutionized samples shows the least negative value of -0.679 ± 0.005 V, followed by As-deposited and Aged samples of the wall. The Aged sample shows the highest negative E_{corr} value of -0.703 ± 0.006 V, whereas the as-deposited sample exhibited a slightly bottom value of -0.697 ± 0.004 V. These observations suggest that solutionizing heat treatment offers a positive influence on the corrosion resistance of the WAAM-deposited alloy, while aging appears to have a detrimental impact. Additionally, Fig. 6.24 shows the digital images and FE-SEM images of the middle region samples before and

after the PDP test. It shows that the area affected by corrosion of the solutionized sample is less than that of the as-deposited and aged samples; more pits are visible on the aged sample; and there is not much difference between the aged and as-deposited samples.

In Fig. 6.24a, FE-SEM images of the as-deposited sample shows numerous silicon carbide impurities which are clearly visible on the surface, along with some pores. In Fig. 6.24b, the grain size appears larger due to heat treatment, and there is a dissolution of impurities occurred, as no visible impurities are present on the surface of the sample. Similarly, in Fig. 6.24c, the grain size remains the same as the solutionized sample, but some impurities of silicon oxide are visible on the surface due to the aging of the sample for 7 days. Figures 6.24 a1, b1, and c1 show the digital images of the as-deposited, solutionized, and aged samples, respectively. From these images, it is clearly visible that the area most affected by corrosion is after aging, and the least affected area is solutionized. This is because solutionizing heat treatment can significantly improve corrosion resistance by promoting the formation of a more uniform passive film on the metal surface. This film acts as a stronger barrier, hindering the corrosion process. Additionally, solutionizing helps create a more uniform microstructure, reducing the areas susceptible to localized attacks by dissolution of beta phase inside the alpha matrix. These combined effects indicate better resistance to corrosion and a bottom corrosion rate. However, after the aging heat treatment, the concentration of the beta phase possibly increases, hindering the formation of a uniform passive film and deteriorating the electrochemical corrosive behavior of the samples. Figures 6.24. a2, b2, and c2 show the FE-SEM images of corroded samples, illustrating differences in pitting areas among all three samples.

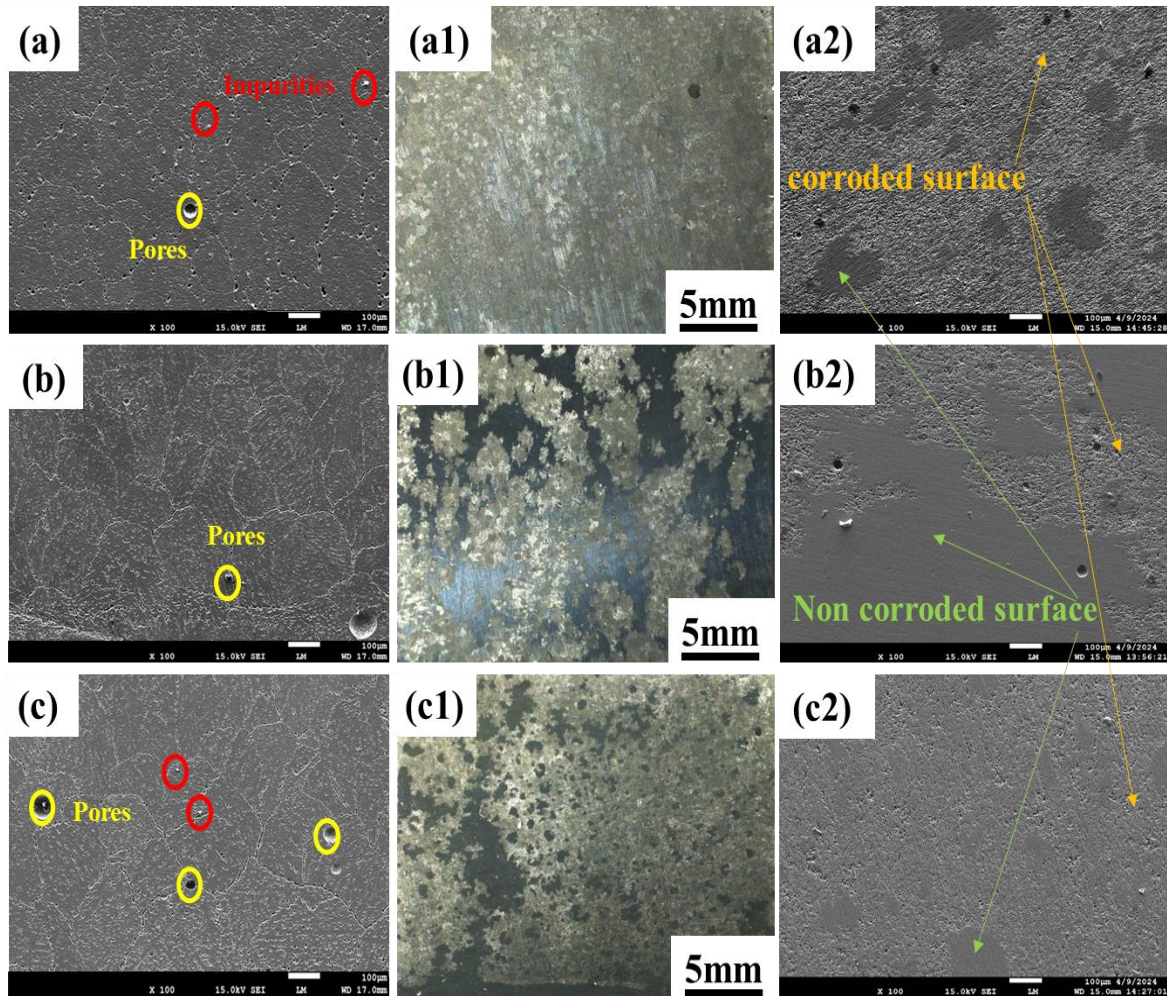


Figure 6.24: FE-SEM images of a) As-deposited b) Solutionized c) Aged samples of middle region and a1), b1) and c1) shows digital images of the same samples; also, a2), b2), and c2) show the FE-SEM images of the corresponding samples, respectively.

Chapter 7

7.1. CONCLUSIONS

This research builds upon established WAAM technology and seeks to assess and enhance the capabilities of components manufactured using ER5356 alloy. Key findings and outcomes of this work are as follows:

- The utilization of Weck's reagent enabled clear visualization of grains within the microstructure. However, the beta phase remains hard to find even with this reagent. It is possible that the beta phase dissolves when reacting with KMnO_4 in Weck's reagent. Despite many attempts, the beta phase could not be observed even through EDS analysis of unetched samples.
- Comparison of XRD results from the literature and experiments revealed identical peak patterns for the alpha phase, demonstrating the reliability of measurements. Slow XRD scan also conducted on the same sample for validation but the results are same.
- EDS mapping and point scanning unveiled the presence of a phase composed of approximately 90% Al and 5% Mg. However, the exact identification of this phase is still under investigation.
- Hardness testing across the sample exhibited minimal variation, with values ranging from 82.82 to 71.72 as one progresses from the bottom to the top. This consistency aligns well with the literature, indicating uniform hardness throughout the sample.
- Heat treatment shows the increment of nearly 15% in hardness upto 82.2HV from 71.72HV.
- Tensile testing reveals that the yield strength (YS) and ultimate tensile strength (UTS) of horizontal samples are higher than those of the vertical samples. Additionally, the yield strength is further increased after the solutionized heat treatment.
- HPT study reveals that hardness of sample is drastically increased upto 1.5 times by using severe plastic deformation in the form of HPT on the sample. This is because of refinement of grains.
- Corrosion testing indicates that the middle section of the wall exhibits the worst pitting resistance, possibly due to a higher concentration of beta phase resulting from increased heat entrapment during wall deposition. Conversely, the top area shows the least pitting resistance, likely due to greater Magnesium loss, increased convection, and reduced heat entrapment. Overall, all the samples demonstrate a maximum of very low

corrosion rate (i.e., 0.097 mm/yr for middle region of aged sample), suggesting that the samples are generally resistant to corrosion.

Additionally, it is observed that after solutionizing, the corrosion resistance of the samples improves. However, when the solutionized samples are aged for up to 7 days, their corrosion resistance deteriorates even further compared to the as-deposited state, likely due to increased beta phase precipitation.

This research effort provides valuable insights into the behavior and characteristics of ER5356 alloy components produced via WAAM technology. Further investigations are required to expand our understanding and refine the manufacturing processes, ultimately contributing to the advancement of additive manufacturing practices and the broader utilization of this alloy across various industries.

7.2. SCOPE OF FUTURE WORK

- **Optimization of Additive Manufacturing Parameters:** Optimize the WAAM process parameters, such as welding speed, travel speed, and heat input, to enhance component quality. Systematically study the effects of these variables on microstructure, mechanical properties, and corrosion resistance.
- **Expansion of Mechanical Testing:** Conduct more tensile testing on multiple samples to obtain a comprehensive dataset. Explore the influence of different orientations, build directions and heat treatment on mechanical performance.
- **Further Characterization of Beta Phase:** Continue investigating the elusive beta phase in ER5356 alloy. Explore alternative etchants or analytical techniques that might reveal its presence and composition. Understanding this phase can provide valuable insights into the material's properties.
- **Corrosion prevention Strategies:** Conducting more experimental potentiostatic and immersion testing to explore potential strategies for mitigating pitting corrosion, especially in the presence of the elusive beta phase. Investigate the effectiveness of various surface treatments, coatings, or alloy modifications to enhance the corrosion resistance of ER5356 alloy components.
- **Comparison with Other Alloys:** Extend the research to compare the WAAM-produced ER5356 alloy with other Aluminium-Magnesium alloys and conventional manufacturing methods. Determine the alloy's competitiveness in terms of both performance and cost-effectiveness.

REFERENCES

- [1] F.M. Mazzolani, Aluminium alloy structures, Pitman Advanced, Boston, London, Melbourne, 1985.
- [2] J.E. Hatch, Aluminium: properties and physical metallurgy, American Society for Metals, 1984.
- [3] Geng, Y., Panchenko, I., Chen, X., Ivanov, Y., & Konovalov, S. V. (2022b). Wire arc additive manufacturing Al-5.0 Mg alloy: Microstructures and phase composition. *Materials Characterization*, 187, 111875.
- [4] L.F. Mondolfo, Aluminium alloys: structure and properties, Elsevier, 2013.
- [5] Wang, J., Zhu, K., Zhang, W., Zhu, X., & Lu, X. (2023). Microstructural and defect evolution during WAAM resulting in mechanical property differences for AA5356 component. *Journal of Materials Research and Technology*, 22, 982–996.
- [6] Su, C., Chen, X., Gao, C., & Wang, Y. (2019). Effect of heat input on microstructure and mechanical properties of Al-Mg alloys fabricated by WAAM. *Applied Surface Science*, 486, 431–440.
- [7] Zhao, D., Long, D., Niu, T., Zhang, T., Hu, X., & Liu, Y. (2022). Effect of MG loss and microstructure on anisotropy of 5356 wire arc additive manufacturing. *Journal of Materials Engineering and Performance*, 31(10), 8473–8482.
- [8] Aluminium Federation. The properties of Aluminium and its alloys, 6th ed., Aluminium Federation, London, 1968.
- [9] Geng, Y., Panchenko, I., Chen, X., Ivanov, Y., & Konovalov, S. (2022b). Wire arc additive manufacturing Al-5.0 Mg alloy: Microstructures and phase composition. *Materials Characterization*, 187, 111875.
- [10] W. Zhang, G. Frankel, Transitions between pitting and intergranular corrosion in AA2024, *Electrochimica Acta*, 48 (2003) 1193-1210.
- [11] Tawfik, M., Nemat-Alla, M., & Dewidar, M. (2021b). Effect of travel speed on the properties of AL-MG Aluminium alloy fabricated by wire arc additive manufacturing. *Journal of Materials Engineering and Performance*, 30(10), 7762–7769.
- [12] Köhler, M., Hensel, J., & Dilger, K. (2020). Effects of thermal cycling on wire and arc additive manufacturing of AL-5356 components. *Metals*, 10(7), 952.
- [13] Köhler, M., Fiebig, S., Hensel, J., & Dilger, K. (2019). Wire and arc additive manufacturing of Aluminium components. *Metals*, 9(5), 608.
- [14] R. Goswami, G. Spanos, P.S. Pao, R.L. Holtz, Precipitation behavior of the beta phase in Al-5083, *Materials science and engineering*, 527 (2010) 1089-1095.
- [15] Yu, Z., Yuan, T., Xu, M., Zhang, H., Jiang, X., & Chen, S. (2021). Microstructure and mechanical properties of Al-Zn-Mg-Cu alloy fabricated by wire + arc additive manufacturing. *Journal of Manufacturing Processes*, 62, 430–439.
- [16] Li, S., Zhang, L., Ning, J., Wang, X., Zhang, G., Zhang, J., Na, S., & Bodaghi, F. (2020). Comparative study on the microstructures and properties of wire+arc additively manufactured 5356 Aluminium alloy with argon and nitrogen as the shielding gas. *Additive Manufacturing*, 34, 101206.

- [17] Fan, S., Guo, X., Li, Z., Ma, J., Li, F., & Jiang, Q. (2023). A review of High-Strength Aluminium-Copper alloys fabricated by Wire Arc Additive Manufacturing: microstructure, properties, defects, and post-processing. *Journal of Materials Engineering and Performance*.
- [18] Kora T Sunny¹, Joby Joseph², Georgekutty S Mangalathu³ & Jeeno Mathew, a review on mechanical & microstructural property evaluation of Aluminium 5083 alloy weldment, vol. 3, issue 4, oct 2013, 119-128.
- [19] Yuan, T., Yu, Z., Chen, S., Xu, M., & Jiang, X. (2020). Loss of elemental Mg during wire + arc additive manufacturing of Al-Mg alloy and its effect on mechanical properties. *Journal of Manufacturing Processes*, 49, 456–462.
- [20] W. Lynes, Some historical developments relating to corrosion, *Journal of the Electrochemical Society*, 98 (1951) C3-C10.
- [21] N. A. Che lah¹, a, m. F. Ahmad ibrahim², b, a. Jalar², c, j. Sharif³, N. K. Othman² and n. M. Rashdi¹, the effect of filler er4043 and er5356 on porosity Distribution of welded aa6061 Aluminium alloy.
- [22] Petru Moldovan¹, Carmen Nicoleta Stanica², Gilbert Ciobanu², Ionel Ungureanu², George Manuel Iorga², Mihai Buțu, intergranular corrosion of aa 5083 - h321 Aluminium alloy, u.p.b. sci. Bull., series b, vol. 76, iss. 3, 2014.
- [23] G.M. Scamans, N.J.H. Holroyd, C.D.S. Tuck, The role of Magnesium segregation in the intergranular stress corrosion cracking of Aluminium alloys, *Corrosion Science*, 27 (1987) 329-347.
- [24] F.J. Esposito, C. Zhang, P.R. Norton, R.S. Timsit, Segregation of Mg to the surface of an Al-Mg single crystal alloy and its influence on the initial oxidation at room temperature, *Surface science*, 302 (1994) 109-120.
- [25] Vishnukumar, M., Pramod, R., & Kannan, A. R. (2021). Wire arc additive manufacturing for repairing Aluminium structures in marine applications. *Materials Letters*, 299, 130112.
- [26] Dobkowska, A., Sotniczuk, A., Bazarnik, P., Mizera, J., & Garbacz, H. (2021). Corrosion behavior of Cold-Formed AA5754 alloy sheets. *Materials*, 14(2), 394.
- [27] Li, S., Dong, H., Shi, L., Li, P., & Ye, F. (2017). Corrosion behavior and mechanical properties of Al-Zn-Mg Aluminium alloy weld. *Corrosion Science*, 123, 243–255.
- [28] Jebaraj, A. V., Aditya, K., Kumar, T., Ajaykumar, L., & Deepak, C. (2020). Mechanical and corrosion behaviour of Aluminium alloy 5083 and its weldment for marine applications. *Materials Today: Proceedings*, 22, 1470–1478.
- [29] N. Ramanaiah² B. Balakrishna, 3 K. Prasad rao, effect of modified aa5356 filler on corrosion behavior of aa6061 alloy GTA welds, vol.2, issue.6, nov-dec. 2012 pp-4429-4433.

- [30] J.A. Lyndon a, R.K. Gupta a, M.A. Gibson b, N. Birbilis a, Electrochemical behaviour of the β -phase intermetallic (Mg_2Al_3) as a function of pH as relevant to corrosion of Aluminium–Magnesium alloys, *Corrosion Science* 70 (2013) 290–293.
- [31] T. Sato, Y. Kojima, T. Takahashi, Modulated structures and GP zones in Al-Mg alloys, *Metallurgical Transactions A*, 13 (1982) 1373-1378.
- [32] M. Van Rooyen, J.S. Maartensdijk, E. Mittemeijer, Precipitation of guinier-preston zones in Aluminium-Magnesium; a calorimetric analysis of liquid-quenched and solid-quenched alloys, *Metallurgical Transactions A*, 19 (1988) 2433-2443.
- [33] M. Starink, A.M. Zahra, β' and β precipitation in an Al–Mg alloy studied by DSC and TEM, *Acta materialia*, 46 (1998) 3381-3397.
- [34] S. Samson, The crystal structure of the phase β Mg_2Al_3 , *Acta Crystallographica*, 19 (1965) 401-413.
- [35] Karayel, E., Bozkurt, Y., Özdemir, C., & Kalender, M. (2022b). Wire Arc Additive Manufacturing Of 5356 Aluminium Alloy. *Research Square (Research Square)*.
- [36] Šćepanović, J. (2018). Investigation of AlMgCu Alloy Corrosion in 0.5M NaCl: Polarization and EIS studies. *International Journal of Electrochemical Science*, 13(9), 8623–8632.
- [37] Gabbardo, A. D., Wang, X., Huggins, A., & Frankel, G. S. (2018). Mechanism of etching of Al-4.5Mg-1.0Mn alloy. *Microscopy and Microanalysis*, 24(4), 374–386.
- [38] Liew, Y., Wijesinghe, S., & Blackwood, D. J. (2021). Investigation of the electrochemical breakdown response in sensitised AA5083 Aluminium alloy. *Sustainability*, 13(13), 7342.
- [39] Król, M., Snopiński, P., Tomiczek, B., Tański, T., Pakieła, W., & Sitek, W. (2016). Structure and properties of an Al alloy in as-cast state and after laser treatment. *Proceedings of the Estonian Academy of Sciences*, 65(2), 107.
- [40] Guan, L., Zhou, Y., Zhang, B., Wang, J., Han, E., & Ke, W. (2016). Influence of aging treatment on the pitting behavior associated with the dissolution of active nanoscale β -phase precipitates for an Al–Mg alloy. *Corrosion Science*, 103, 255–267.
- [41] C.A. Smith, Corrosion story .3. Zinc, Lead and Aluminium, *Anti-Corrosion Methods and Materials*, 24 (1977) 13-15.
- [42] M. Pourbaix, Atlas of electrochemical equilibria in aqueous solutions, National Association of Corrosion Engineers, 1974.
- [43] R.H. Jones, Stress corrosion cracking: materials performance and evaluation, ASM International, Ohio, 1992.

- [44] Król, M., Snopiński, P., Tomiczek, B., Tański, T., Pakieła, W., & Sitek, W. (2016). Structure and properties of an Al alloy in as-cast state and after laser treatment. *Proceedings of the Estonian Academy of Sciences*, 65(2), 107.
- [45] Guan, L., Zhou, Y., Zhang, B., Wang, J., Han, E., & Ke, W. (2016). Influence of aging treatment on the pitting behavior associated with the dissolution of active nanoscale β -phase precipitates for an Al–Mg alloy. *Corrosion Science*, 103, 255–267.
- [46] Révész, Á., & Gajdics, M. (2021). High-Pressure Torsion of Non-Equilibrium Hydrogen Storage Materials: A review. *Energies*, 14(4), 819.
- [47] F. Andreatta, H. Terryn, J. De Wit, Corrosion behaviour of different tempers of AA7075 Aluminium alloy, *ElectrochimicaActa*, 49 (2004) 2851-2862.
- [48] Z.S. Smialowska, Pitting Corrosion of Metals, National Assn of Corrosion Engineers, 1986.
- [49] N. Birbilis, R. Buchheit, Electrochemical characteristics of intermetallic phases in Aluminium alloys an experimental survey and discussion, *Journal of The Electrochemical Society*, 152 (2005) B140-B151.
- [50] G.S. Frankel, Z. Xia, Localized corrosion and stress corrosion cracking resistance of friction stir welded Aluminium alloy 5454, *Corrosion*, 55 (1999) 139-150.
- [51] R. Baboian, Corrosion tests and standards: Application and interpretation (2nd Edition): (MNL 20), in, ASTM International.
- [52] M.L.C. Lim, J.R. Scully, R.G. Kelly, Intergranular corrosion penetration in an Al-Mg alloy as a function of electrochemical and metallurgical conditions, *Corrosion*, 69 (2013).
- [53] J. Galvele, S. de De Micheli, Mechanism of intergranular corrosion of Al-Cu alloys, *Corrosion Science*, 10 (1970) 795-807.
- [54] E.H. Dix Jr, W.A. Anderson, M.B. Shumaker, Influence of service temperature on the resistance of wrought Aluminium-Magnesium alloys to corrosion, *Corrosion*, 15 (1959) 19-26.
- [55] J.R. Davis, Corrosion of Aluminium and Aluminium alloys, in, ASM International, 1999.
- [56] R.H. Jones, ASM handbook -corrosion: fundamentals, testing and protection, 13A, p. 345, ASM International, Materials Park, OH, (2003).
- [57] E.H. Hollingsworth, H.Y. Hunsicker, Metals handbook 9th edition-corrosion, ASM International, Materials Park, OH, 1987.
- [58] J.C. Chang, T.H. Chuang, The degradation of corrosion resistance for Al 5083 alloy after thermal and superplastic forming processes, *Journal of Materials Engineering and Performance*, 9 (2000) 253-260.

- [59] Standard specification for Aluminium and Aluminium-alloy sheet and plate (metric), ASTM B209M-14, (2014).
- [60] I.N.A. Oguocha, O.J. Adigun, S. Yannacopoulos, Effect of sensitization heat treatment on properties of Al-Mg alloy AA5083-H116, *Journal of Materials Science*, 43 (2008) 4208-4214.
- [61] J.L. Searles, P.I. Gouma, R.G. Buchheit, Stress corrosion cracking of sensitized AA5083 (Al-4.5Mg-1.0Mn), in: P.J. Gregson, S.J. Harris (Eds.) *Aluminium Alloys 2002: Their Physical and Mechanical Properties Pts 1-3*, Trans Tech Publications Ltd, Zurich-Uetikon, 2002, pp. 1437-1442.
- [62] Nagasai, B. P., Malarvizhi, S., & Balasubramanian, V. (2022). Mechanical properties and microstructural characteristics of AA5356 Aluminium alloy cylindrical components made by Wire Arc Additive Manufacturing process. *Materials Performance and Characterization*, 11(1), 20210132.
- [63] Zhao, D., Long, D., Niu, T., Zhang, T., Hu, X., & Liu, Y. (2022). Effect of MG loss and microstructure on anisotropy of 5356 wire arc additive manufacturing. *Journal of Materials Engineering and Performance*, 31(10), 8473–8482.
- [64] Zuo, W., Ma, L., Yu, L., Li, S., Ji, Z., & Deng, M. (2018). Effects of solution treatment temperatures on microstructure and mechanical properties of TIG–MIG hybrid arc additive manufactured 5356 Aluminium alloy. *Metals and Materials International*, 24(6), 1346–1358.
- [65] Geng, Y., Panchenko, I., Chen, X., Ivanov, Y., & Konovalov, S. V. (2021). Investigation of microstructure and fracture mechanism of Al-5.0MG alloys fabricated by wire arc additive manufacturing. *Journal of Materials Engineering and Performance*, 30(10), 7406–7416.
- [66] Utyaganova, V. R., Filippov, A. V., Tarasov, S. Y., Shamarin, N. N., Gurianov, D. A., Vorontsov, A. V., Chumaevskii, A. V., Fortuna, S. V., Savchenko, N. L., Rubtsov, V. E., & Kolubaev, E. A. (2021). Characterization of AA7075/AA5356 gradient transition zone in an electron beam wire-feed additive manufactured sample. *Materials Characterization*, 172, 110867.
- [67] Karayel, E., Bozkurt, Y., ÖzdemiR, C., & Kalender, M. (2022). Wire Arc Additive Manufacturing Of 5356 Aluminium Alloy. *Research Square (Research Square)*.
- [68] Kora T Sunny¹, Joby Joseph², Georgekutty S Mangalathu³& Jeeno Mathew, a review on mechanical & microstructural property evaluation of Aluminium 5083 alloy weldment, vol. 3, issue 4, oct 2013, 119-128.
- [69] T.X. Gao, H.M. Liu, F.Y. Wang and Y. Chen, Effect of Ce on the Microstructure and Mechanical Properties of 5356 Aluminium Alloy, *Mater. Sci. Technol.*, 2016, 24(3), p 34–39.

- [70] Kim, G., Kim, D., Hwang, I., Kim, D., Kim, Y., & Park, J. (2021). Mechanical Properties of Aluminium 5083 Alloy GMA Welds with Different Magnesium and Manganese Content of Filler Wires. *Applied Sciences*, 11(24), 11655.
- [71] N. A. Che lah1, a, m. F. Ahmad ibrahim2, b, a. Jalar2, c, j. Sharif 3, N. K. Othman2 and n. M. Rashdi1, the effect of filler er4043 and er5356 on porosity Distribution of welded aa6061 Aluminium alloy.
- [72] Petru moldovan1, carmen nicoleta stanica2, gilbert ciobanu2, ionel Ungureanu2, george manuel iorga2, mihai buțu, intergranular corrosion of aa 5083 - h321 Aluminium alloy, u.p.b. sci. Bull., series b, vol. 76, iss. 3, 2014.
- [73] Liu, Z., Sun, J., Yan, Z., Lin, Y., Liu, M., Roven, H. J., & Dahle, A. K. (2021). Enhanced ductility and strength in a cast Al–Mg alloy with high Mg content. *Materials Science and Engineering A-structural Materials Properties Microstructure and Processing*, 806, 140806.
- [74] S. Nebti, D. Hamana, G. Cizeron, Calrimetric study of preprecipitation and precipitation in Al-Mg alloy, *Acta Metallurgica Et Materialia*, 43 (1995) 3583-3588.
- [75] Vishnukumar, M., Pramod, R., & Kannan, A. R. (2021). Wire arc additive manufacturing for repairing Aluminium structures in marine applications. *Materials Letters*, 299, 130112.
- [76] Dobkowska, A., Sotniczuk, A., Bazarnik, P., Mizera, J., & Garbacz, H. (2021). Corrosion behavior of Cold-Formed AA5754 alloy sheets. *Materials*, 14(2), 394.
- [77] Li, S., Dong, H., Shi, L., Li, P., & Ye, F. (2017). Corrosion behavior and mechanical properties of Al-Zn-Mg Aluminium alloy weld. *Corrosion Science*, 123, 243–255.
- [78] Jebaraj, A. V., Aditya, K., Kumar, T., Ajaykumar, L., & Deepak, C. (2020). Mechanical and corrosion behaviour of Aluminium alloy 5083 and its weldment for marine applications. *Materials Today: Proceedings*, 22, 1470–1478.
- [79] N. Ramanaiah 2 B. Balakrishna, 3 K. Prasad rao, effect of modified aa5356 filler on corrosion behavior of aa6061 alloy GTA welds, vol.2, issue.6, nov-dec. 2012 pp-4429-4433.
- [80] J.A. Lyndon a, R.K. Gupta a, M.A. Gibson b, N. Birbilis a, Electrochemical behaviour of the b-phase intermetallic (Mg₂Al₃) as a function of pH as relevant to corrosion of Aluminium–Magnesium alloys, *Corrosion Science* 70 (2013) 290–293.
- [81] Utyaganova, V. R., & Shamarin, N. N. (2020). Investigation of corrosion properties of electron beam additive manufactured AA5356. *Nucleation and Atmospheric Aerosols*.
- [82] Sander, G., Tan, J. K., Balan, P., Gharbi, O., Feenstra, Singer, L. E., Thomas, S., Kelly, R. G., Scully, J. R., & Birbilis, N. (2018). Corrosion of additively manufactured alloys: a review. *Corrosion*, 74(12), 1318–1350.

- [83] Geng, Y., Panchenko, I., Chen, X., Ivanov, Y., & Konovalov, S. V. (2022). Wire arc additive manufacturing Al-5.0 Mg alloy: Microstructures and phase composition. *Materials Characterization*, 187, 111875.
- [84] Badr Kamoon†*, Salam Abeed Dahe‡ & Zuhair H. Obaid, Microstructural Evaluation for TIG Welding of AA6061-T6 using ER5356 Filler Metal; in Postweld and as-Weld Treatment, *Vol. 43, No. 2, pp. 154-164*.
- [85] Karayel, E., Bozkurt, Y., Özdemir, C., & Kalender, M. (2022b). Wire Arc Additive Manufacturing Of 5356 Aluminium Alloy. *Research Square (Research Square)*.
- [86] Šćepanović, J. (2018). Investigation of AlMgCu Alloy Corrosion in 0.5M NaCl: Polarization and EIS studies. *International Journal of Electrochemical Science*, 13(9), 8623–8632.
- [87] Gabbardo, A. D., Wang, X., Huggins, A., & Frankel, G. S. (2018). Mechanism of etching of Al-4.5Mg-1.0Mn alloy. *Microscopy and Microanalysis*, 24(4), 374–386.
- [88] Liew, Y., Wijesinghe, S., & Blackwood, D. J. (2021). Investigation of the electrochemical breakdown response in sensitised AA5083 Aluminium alloy. *Sustainability*, 13(13), 7342.